

The INT Photometric H α Survey of the Northern Galactic Plane (IPHAS)

Janet E. Drew,^{1*} R. Greimel,² M. J. Irwin,³ A. Aungwerojwit,⁴ M. J. Barlow,⁵
 R. L. M. Corradi,² J. J. Drake,⁶ B. T. Gänsicke,⁴ P. Groot,⁷ A. Hales,⁵ E. C. Hopewell,¹
 J. Irwin,³ C. Knigge,⁸ P. Leisy,^{9,2} D. J. Lennon,² A. Mampaso,⁹ M. R. W. Mashedier,¹⁰
 M. Matsuura,¹¹ L. Morales-Rueda,⁷ R. A. H. Morris,¹⁰ Q. A. Parker,^{12,13} S. Phillipps,¹⁰
 P. Rodriguez-Gil,^{4,9} G. Roelofs,⁷ I. Skillen,² J. L. Sokoloski,⁶ D. Steeghs,⁶
 Y. C. Unruh,¹ K. Viironen,⁹ J. S. Vink,¹ N. A. Walton,³ A. Witham,⁸ N. Wright,⁵
 A. A. Zijlstra¹¹ and A. Zurita¹⁴

¹Imperial College of Science, Technology and Medicine, Blackett Laboratory, Exhibition Road, London, SW7 2AZ

²Isaac Newton Group of Telescopes, Apartado de correos 321, E-38700 Santa Cruz de la Palma, Tenerife, Spain

³Institute of Astronomy, Cambridge University, Madingley Road, Cambridge, CB3 0HA

⁴Department of Physics, University of Warwick, Coventry, CV4 7AL

⁵University College London, Department of Physics & Astronomy, Gower Street, London, WC1E 6BT

⁶Harvard-Smithsonian Center for Astrophysics, 60 Garden Street, Cambridge, MA 02138, USA

⁷Afdeling Sterrenkunde, Radboud Universiteit Nijmegen, Faculteit NWI, Postbus 9010, 6500 GL Nijmegen, the Netherlands

⁸School of Physics & Astronomy, University of Southampton, Southampton, SO17 1BJ

⁹Instituto de Astrofísica de Canarias, 38200 La Laguna, Tenerife, Spain

¹⁰Astrophysics Group, Department of Physics, Bristol University, Tyndall Avenue, Bristol, BS8 1TL

¹¹School of Physics and Astronomy, University of Manchester, Sackville Street, PO Box 88, Manchester, M60 1QD

¹²Department of Physics, Macquarie University, NSW 2109, Australia

¹³Anglo-Australian Observatory, PO Box 296, Epping NSW 1710, Australia

¹⁴Departamento de Física Teórica y del Cosmos, Facultad de Ciencias, Avd. Fuentenueva S/N, Granada, 18071, Spain

Accepted 2005 June 20. Received 2005 June 14; in original form 2005 April 25

ABSTRACT

The Isaac Newton Telescope (INT) Photometric H α Survey of the Northern Galactic Plane (IPHAS) is a 1800-deg² CCD survey of the northern Milky Way spanning the latitude range $-5^\circ < b < +5^\circ$ and reaching down to $r' \simeq 20$ (10σ). Representative observations and an assessment of point-source data from IPHAS, now underway, are presented. The data obtained are Wide Field Camera images in the H α narrow-band, and Sloan r' and i' broad-band filters. We simulate IPHAS ($r' - H\alpha$, $r' - i'$) point-source colours using a spectrophotometric library of stellar spectra and available filter transmission profiles: this defines the expected colour properties of (i) solar metallicity stars, without H α emission, and (ii) emission-line stars. Comparisons with observations of fields in Aquila show that the simulations of normal star colours reproduce the observations well for all spectral types earlier than M. A further comparison between colours synthesized from long-slit flux-calibrated spectra and IPHAS photometry for six objects in a Taurus field confirms the reliability of the pipeline calibration. Spectroscopic follow-up of a field in Cepheus shows that sources lying above the main stellar locus in the ($r' - H\alpha$, $r' - i'$) plane are confirmed to be emission-line objects with very few failures. In this same field, examples of H α deficit objects (a white dwarf and a carbon star) are shown to be readily distinguished by their IPHAS colours. The role IPHAS can play in studies of spatially resolved northern Galactic nebulae is discussed briefly and illustrated by a continuum-subtracted mosaic image of Shajn 147 (a supernova remnant, 3° in diameter). The final catalogue of IPHAS point sources will contain photometry on about 80 million objects. Used on its own, or in combination with near-infrared photometric catalogues, IPHAS is a major resource for the study of stellar populations making up the disc of the Milky Way. The eventual yield of new northern

*E-mail: j.drew@imperial.ac.uk

emission-line objects from IPHAS is likely to be an order of magnitude increase on the number already known.

Key words: surveys – stars: emission-line, Be – stars: general – Galaxy: disc – Galaxy: stellar content.

1 INTRODUCTION

The astronomical significance of $H\alpha$ spectral line emission is that it both traces diffuse ionized nebulae and is commonly prominent in the spectra of pre- and post-main-sequence stars and binaries. Because these are objects in relatively short-lived phases of evolution, they are a minority in a mature galaxy like our own. Their scarcity has in turn acted as a brake on our understanding of these crucial evolutionary stages that in youth help shape the growth of planetary systems, and in old age determine stellar end states and the recycling of energy and chemically enriched matter back into the galactic environment. The major groups of emission-line stars include all evolved massive stars (supergiants, luminous blue variables, Wolf–Rayet stars, various types of Be star), post-asymptotic giant branch (AGB) stars, pre-main-sequence stars at all masses, active stars and interacting binaries. This last group most likely harbours Type Ia supernova (SN Ia) progenitors within it, in guises that are still subject to considerable debate (Hillebrandt & Niemeyer 2000; Uenishi, Nomoto & Hachisu 2003).

Existing catalogues of emission-line objects contain anything from a few, to a few hundred, sources. Within the least populous object classes (e.g. the luminous blue variables and supersoft X-ray binaries, with just a few of each known in the Galaxy), there can be a confusing *mêlée* of ‘special cases’ that inhibit confident identification of essential and general behaviours. In effect, stellar evolutionary studies have been bedevilled by small-number statistics and a lack of good demographics. The remedy for this problem is to exploit the technical developments of recent years that have boosted both the efficiency with which large-scale astronomical surveys can be performed and the quality that can be achieved. In particular, large area CCD-mosaic detectors offering good spatial resolution have now completely supplanted the photographic techniques of the last century. In this paper, we describe the Isaac Newton Telescope (INT) Photometric $H\alpha$ Survey of the Northern Galactic Plane (IPHAS), a programme that began taking data with the INT Wide Field Camera (WFC) in the second half of 2003.

The goal of IPHAS is to survey the entire northern Galactic plane in the latitude range $-5^\circ < b < +5^\circ$: a sky area of 1800 deg^2 . The choice of latitude range was tensioned between the rising total telescope time requirement and the expected fall off in discoveries to be made with increasing latitude (see below). The 10° -wide strip requires in the region of 22 weeks clear time and the hope is to complete the observations before the end of 2006. The data obtained will be mined both for spatially resolved nebulae and for unresolved emission-line stars. For point sources, the magnitude range will be $13 \lesssim r' \lesssim 20$. Here, we will focus on presenting the basic features of the survey, together with the extraction of point-source data and the analysis of photometric colour information. The different technical issues relating to the identification and measurement of resolved $H\alpha$ -emitting nebulae will be presented in a later paper. For now, we just point to the opportunity that IPHAS presents both for making new discoveries and for high-quality $H\alpha$ emission mapping on large angular scales.

To place this new Northern hemisphere survey in context, it is appropriate to review the scale and character of the emission-line star population that previous Galactic $H\alpha$ surveys have revealed. Kohoutek & Wehmeyer (1999, hereafter KW99) have added their own discoveries within the latitude range $-10^\circ < b < +10^\circ$ (1979 objects; data obtained in the years 1964–1970) to those of a wide range of independent searches: these go back as far as the original work of Merrill & Burwell that resulted in the Mount Wilson Catalogue (MWC; see Merrill & Burwell 1933). The total number of KW99 objects is 4174. In many cases, the source observations are spectra obtained using objective prism facilities. For sources in the Northern hemisphere, this compilation supersedes that due to Wackerling (1970). Three-quarters of the stars listed in KW99 are assigned a photovisual magnitude, $m_{pv} < 13$ and it is surmised that this is roughly the completeness limit of the catalogue. They also note that over 80 per cent of all the objects they list in the $-10^\circ < b < +10^\circ$ band fall within the narrower $-5^\circ < b < +5^\circ$ band. At the fainter magnitudes we are exploring, we might expect this concentration towards the Galactic Equator to become even more pronounced. Naive extrapolation of the bright-end ($m_{pv} < 13$) magnitude distribution of the KW99 emission-line stars to span $13 < m_{pv} < 20$ would suggest that our survey should uncover 8000–10 000 new objects.

This is probably an underestimate for a number of reasons. First, we can check this extrapolation of KW99 against the same quantity derived from the Stephenson & Sanduleak (1971, hereafter SS71) southern Galactic plane survey. The SS71 completeness limit is shallower at $m_{pg} \sim 11$. We find, even on excluding the Galactic bulge region located exclusively in the southern sky, that the prediction rises to $\sim 40\,000$. This dramatic difference can have a number of origins: beginning with simple differences in the Galactic stellar populations accessible from the Northern and Southern hemispheres, and ending with issues of experimental technique. Nevertheless, a parallel between the KW99 and SS71 catalogues is that the bright magnitudes sampled strongly favour early-type, intrinsically luminous stars (such objects account for three-quarters of the KW99 catalogue). Moving towards much fainter magnitudes, the sampled emission-line star population is likely to broaden in character as intrinsically fainter object types (e.g. young and active stars, interacting binaries) become included.

An immediate precursor to IPHAS and, indeed, a prompt for the need for a northern survey is the Anglo-Asutrialian Observatory UK Schmidt Telescope (UKST) narrow-band $H\alpha$ Survey of the Southern Galactic Plane and Magellanic Clouds. This was the last photographic sky survey carried out on the UKST. It was completed in 2003 and is now available as digital survey data derived from SuperCOSMOS scans of the original SuperCOSMOS H-alpha Survey (SHS) data base, located at <http://www-wfau.roe.ac.uk/ss/halpha/>. A description of this survey is presented by Parker et al. (2005). Important points to note are its high spatial resolution (~ 1 arcsec) and its areal completeness: the entire southern Galactic plane was imaged within the latitude range $-10^\circ < b < +10^\circ$. Each of the 233 Galactic plane fields observed had an effective dimension projected

Table 1. Coordinates of centres, estimates of maximum Galactic reddenings, observation dates and seeing for the IPHAS fields discussed in this paper. Note that the offset partner field (nnno to field nnnn) is offset by 5-arcmin N and 5-arcmin E. The reddening estimates are derived from the Schlegel et al. (1998) reddening maps.

IPHAS field number	Field centre coordinates				Maximum reddening [$E(B - V)$]	Observation date (dd/mm/yyyy)	Mean seeing (arcsec)	
	RA (2000)	Dec. (2000)	ℓ ($^\circ$)	b ($^\circ$)				
2540	05 ^h 33 ^m 49 ^s	+25 $^\circ$ 15'	181.73	-4.18	1.1	05/11/2003	0.8	Section 2, 5
4090	18 ^h 32 ^m 03 ^s	+00 $^\circ$ 41'	31.33	+4.62	2.3	09/06/2004	1.1	Section 3
4095	18 ^h 33 ^m 33 ^s	+01 $^\circ$ 47'	32.48	+4.79	1.6	09/06/2004	1.0	Section 3, 4
4199	18 ^h 47 ^m 27 ^s	+01 $^\circ$ 58'	34.23	+1.78	3.0	12/06/2004	0.9	Section 3, 4
6985	22 ^h 14 ^m 56 ^s	+61 $^\circ$ 11'	105.18	+3.83	2.3	05/11/2003	0.8	Section 6
6993	22 ^h 15 ^m 56 ^s	+61 $^\circ$ 44'	105.59	+4.21	2.5	05/11/2003	0.8	Section 6
7012	22 ^h 18 ^m 36 ^s	+61 $^\circ$ 22'	105.65	+3.73	1.8	03/11/2003	1.2	Section 6
7019	22 ^h 19 ^m 39 ^s	+61 $^\circ$ 55'	106.06	+4.12	2.4	03/11/2003	1.2	Section 6

on the sky of $4^\circ \times 4^\circ$. The southern survey has provided the source material for a variety of continuing research projects (see e.g. Morgan, Parker & Russeil 2001; Parker & Morgan 2003; Drew et al. 2004). For the detection of point sources, IPHAS betters both the SHS sensitivity and spatial resolution, and offers the advantage of CCD dynamic range and linearity. The sensitivity of the two surveys to spatially resolved $H\alpha$ emission is comparable.

We begin the description of IPHAS in the next section with a presentation of the filters used, and our observing and data reduction techniques. Following this, in Section 3, we discuss the use of the $H\alpha, r', i'$ filter photometry in the diagnostic ($r' - H\alpha$) versus ($r' - i'$) diagrams that can be constructed from the survey data for point sources. Specifically, we introduce simulated colour–colour tracks for both normal solar metallicity stars occupying the main stellar locus and for emission-line objects. We then provide examples of ($r' - H\alpha, r' - i'$) diagrams in three contrasting northern Galactic plane locations (Sections 4 to 6). The fields discussed are identified in Table 1. In Section 4, we illustrate the application of the simulated tracks for normal stars with reference to fields in Aquila; in Section 5, we perform a consistency check of IPHAS photometry of a Taurus field obtained on a photometric night; and, in Section 6, we present some follow-up spectroscopy relating to a field in Cepheus that illustrates the high success rate achieved in the confirmation of candidate emission-line objects. In Section 7, we outline the application of IPHAS to imaging spatially resolved nebulae and illustrate this with the beautiful example of the supernova remnant, S 147. The paper ends with a summarizing discussion (Section 8).

2 SURVEY OBSERVATIONS AND DATA EXTRACTION

2.1 IPHAS observations

The WFC, mounted on the 2.5-m INT, is an imager comprising four anti-reflection-coated, thinned $4k \times 2k$ EEV CCDs arranged in an L shape, capturing data from an on-sky area of approximately 0.3 deg^2 . With a pixel dimension of $13.5 \mu\text{m}$, corresponding on-sky to $0.333 \times 0.333 \text{ arcsec}^2$, the instrument is appropriately configured to fully exploit the high-quality subarcsecond seeing frequently encountered at the Roque de los Muchachos Observatory in La Palma. Adequately sampled ~ 1 -arcsec resolution is particularly useful given that lower-reddening Galactic plane star fields, observed down to ~ 20 th magnitude, are at times very crowded.

Not accounting for the geometric consequences of the L-shaped detector arrangement, the total number of pointings required to span

the $10 \times 180 \text{ deg}^2$ survey area would be 6000. On accounting for the detector outline and requiring a little overlap between pointings, we have chosen to fix the number of field centres at a total of 7635. Furthermore, each pointing is paired with a second pointing at an offset of 5-arcmin W and 5-arcmin S, such that the number of quality-controlled sets of exposures expected to be compiled into the final survey data base is 15 270. Stars falling into a gap between the mosaicked CCDs in one exposure are captured in a partner exposure set. Nevertheless, the great majority of Galactic plane sources will be imaged at least twice. The pairing and offsetting, together with the chosen tessellation, come very close to complete coverage of the northern plane (>99 per cent).

Because $H\alpha$ falls in the red part of the spectrum, IPHAS was conceived of as a large-scale programme that could readily make use of less heavily subscribed bright and grey nights. To ensure this scheduling flexibility, whilst obtaining the associated continuum-band observations required for establishing unambiguous $H\alpha$ excesses, it was decided to restrict our broad-band choices to red or longer wavelengths. This also has the effect of increasing the penetration of the survey for a given exposure time because these longer wavelengths are also less subject to Galactic dust obscuration than UBV bands. This stands in contrast to the somewhat bluer emphases of the older $H\alpha$ catalogues (e.g. SS71, where the objective prism data spanned $3300 < \lambda(\text{\AA}) < 6800$). The particular choice we made was to obtain the $H\alpha$ exposures alongside Sloan r' and i' filter observations.

All three filter profiles are plotted as Fig. 1. The Sloan filters have been preferred over Harris alternatives because of their squarer transmission profiles. The Sloan r' filter is the most blue sensitive of the three (central wavelength 6240 \AA), with the $H\alpha$ filter positioned towards the red end of its bandpass (central wavelength 6568 \AA). With an FWHM transmission of 95 \AA , the $H\alpha$ filter is more than broad enough to capture all likely Doppler shifts due to Galactic motions of up to a few hundred km s^{-1} or $\sim 10 \text{ \AA}$, as well as blueshifts of up to an additional $\sim 10 \text{ \AA}$ due to the converging beam of the INT/WFC. The central wavelength of the Sloan i' filter is 7743 \AA . We have added two broad-band filters to this survey in order to give a continuum-dominated colour with which the ($r' - H\alpha$) excess measurement can be compared. It has been shown in the past (see e.g. Robertson & Jordan 1989) that this is important for distinguishing between a genuine $H\alpha$ emission excess and a molecular band dominated late-type stellar spectrum: in such cases, large ($r' - H\alpha$) ‘colour’ will correlate with relatively extreme ($r' - i'$). In truth, the diagnostic value of this strategy is wider than this, as shall become apparent in Section 3.

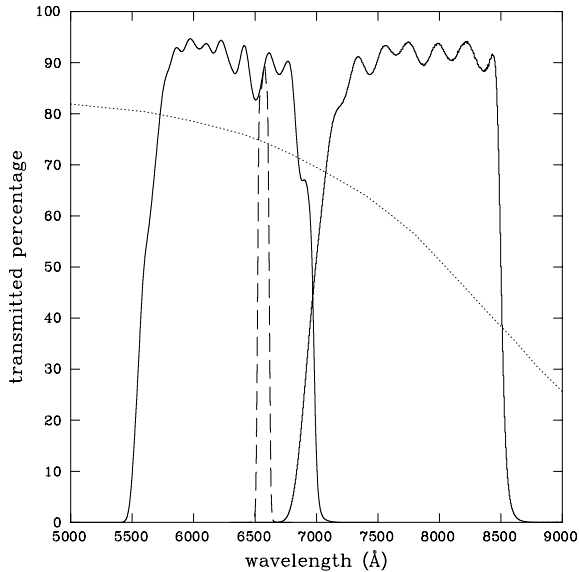


Figure 1. The transmission profiles of the $H\alpha$, Sloan r' and i' filters used in all IPHAS observations. The r' and i' filter profiles are plotted as solid lines, whilst the $H\alpha$ profile is shown dashed. The dotted line is the mean WFC CCD response at the cooled working temperature. These profiles are available in numerical form from the INT/WFC web page (<http://www.ing.iac.es/quality/filter/filt4.html>).

The exposure times in the three filters were set at 120 s ($H\alpha$) and 10 s (r' and i') for observing of the first season in 2003. Evaluation of these data, once extracted, led us to increase the r' -band exposure to 30 s, from the start of the 2004 observing season, to compensate better for their typically higher moonlit background. This adjustment also acknowledges the pivotal role the r' -band exposures must play in the exploitation of the survey: it is important that errors in this band, appearing in both the $H\alpha$ excess and the broad-band colour measurement, are minimized.

For the purpose of photometric calibration, the observations of each night include standard fields, obtained in twilight and at intervals of approximately 2 h through the night. The standards are chosen from a list including the Landolt equatorial fields (Landolt 1992), Sloan (Smith et al. 2002) and Stetson standards (at the Canadian Astronomy Data Centre, <http://cadwww.dao.nrc.ca/standards/>). Nightly observations are also acquired of spectrophotometric standards with a view to assisting the final calibration of the narrow-band $H\alpha$ data. A programme of supporting spectrophotometric observations is planned with a view to placing the $H\alpha$ calibration on the desired firm footing in the longer term.

2.2 Data processing

Processing of IPHAS INT WFC data generally follows the pipeline procedure devised by Irwin & Lewis (2001) for dealing with optical mosaic camera data. The 2D instrumental signature removal includes provision for: non-linearity correction at the detector level; bias and overscan correction prior to trimming to the active detector areas; flat-fielding; and fringe removal in the i' passband.

Flat-fielding in all bands is accomplished by stacking suitable twilight flat-field exposures taken over the course of each, typically 1-week, observing run to create master calibration flats. These have been found to be stable on this time-scale provided no filter changes, or other instrumental set-up changes, occur in the middle of the run. The gain differences between each detector in each passband are

removed by normalizing a robust measure of the average sky level for each detector to a common system (in this case, the sky level on CCD no. 1). The flat-fielded i' data, even for the short exposures (10 s) used here, show measurable fringing. At the same time, the data taken for the IPHAS project are not themselves suitable (short exposures in crowded Galactic plane regions) to construct good quality fringe maps for correcting this problem. Because the fringing in the i' band is relatively stable with time, we make use of a library of i' -band fringe maps taken from other observing runs using the INT WFC. These have been found to reduce the level of fringing to an acceptable level when used with the defringing algorithm in the pipeline.

Each master flat, in conjunction with a previously defined bad column list, is also used to construct confidence maps for each passband. These are used during the catalogue generation to flag less reliable pixels in each image by providing a measure of the inverse variance weight for each pixel, e.g. bad pixels have zero weight, heavily vignetted regions have low weight, reduced sensitivity pixels have lower weight and so on. These confidence measures are used directly to weight the image detection part of the catalogue generation algorithm and help avoid generating excessive numbers of spurious images around defects and other excessively noisy regions.

Catalogue generation follows the precepts outlined by Irwin (1985, 1997) and includes the facility to: automatically track any background variations on scales of typically 20–30 arcsec; detect and deblend images or groups of images; and parametrize the detected images to give various (soft-edged) aperture fluxes, position and shape measures. The generated catalogues start with an approximate World Coordinate System (WCS) defined by the known telescope and camera properties (e.g. WCS distortion model) and are then progressively refined using all-sky astrometric catalogues [e.g. those of the United States Naval Observatory (USNO), the Automated Plate Measurement (APM) and the Two-Micron All Sky Survey (2MASS)] to give internal precision generally better than 0.1 arcsec, and global external precision of 0.25 arcsec with respect to USNO and APM, and 0.1 arcsec with respect to 2MASS. These latter numbers are solely dependent on the accuracy of the astrometric catalogues used in the refinement.

All catalogues for all CCDs for each pointing are then processed using the image shape parameters for morphological classification in the main categories: stellar; non-stellar; noise-like. A sampled curve of growth for each detected object is derived from a series of aperture flux measures as a function of radius. The classification is then based on comparing the curve of growth of the flux for each detected object with the well-defined curve of growth for the general stellar locus. The latter is a direct measure of the integral of the point spread function (PSF) out to various radii and is independent of magnitude, if the data are properly linearized and if saturated images are excluded. The average stellar locus on each detector is clearly defined and is used as the basis for a null hypothesis stellar test for use in classification. The curve of growth for stellar images is also used to automatically estimate frame-based aperture corrections for conversion to total flux.¹

Any photometric standards observed during the run (mainly Landolt 1992 and spectrophotometric standards) are automatically

¹ We note that in regions of intense nebular emission with increasingly short spatial scale variations of the ‘background’, automatic detection, parametrization and classification of objects becomes progressively more unreliable. In such regions, continuum subtraction via difference imaging will yield better results.

located in a standards data base and used to estimate the zero-point in each passband for every pointing containing any of these standards. The trend in the derived zero-points is then used to assign a photometric quality index for each night and also as a first pass estimate for the magnitude calibration for all the observations. The H α filter is treated as equivalent to a standard Johnson–Cousins R -band filter to obtain a Vega-like magnitude, which is used as an initial calibration (to be refined later, as mentioned above).

Various quality control plots are generated by the pipeline and these are used to monitor characteristics, such as: the seeing; the average stellar image ellipticity (to measure trailing); the sky brightness and sky noise; the size of aperture correction for use with the ‘optimal’ aperture flux estimates (here, ‘optimal’ refers to the well-known property that soft-edged apertures of roughly the average seeing radius provide close to profile fit accuracy, e.g. Naylor 1998). The ‘optimal’ catalogue fluxes for the r' , i' and H α filters for each field are then combined to produce a single matched merged catalogue from which diagnostic colour–magnitude diagrams and two-colour diagrams may be produced. These merged catalogues (the fundamental IPHAS product) contain flux, classification and match position error for each object in each passband.

The International Astronomical Union-registered naming convention for all point sources derived from these catalogues is IPHAS JHHMMSS.ss+DDMMSS.s: thereby encoding the 2000 object coordinates into the name.

To give an impression of the internal magnitude errors in the catalogued magnitudes and derived colours we plot, in Fig. 2, the rms deviation between the magnitudes measured in each filter, and the associated colours, for point sources common to two overlapping exposure sets (fields 2540 and 2540o, discussed again in Section 5). These were obtained on a photometric night in 2003 November as the

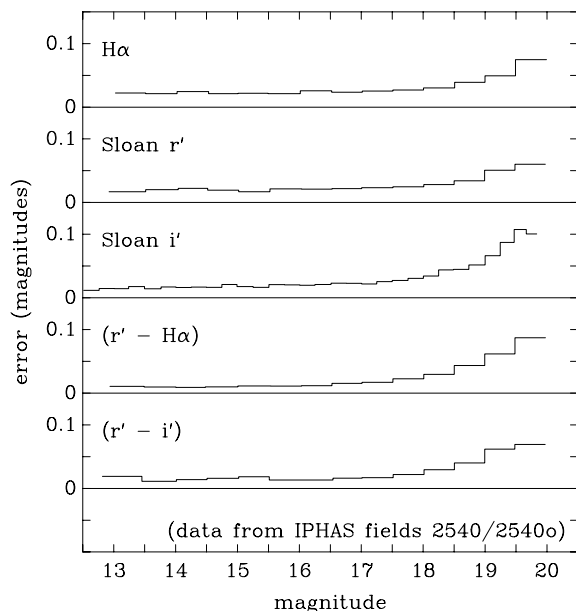


Figure 2. Magnitude and colour errors in IPHAS data as a function of magnitude. The quantity shown, for each filter in the top three panels, is the rms deviation per magnitude bin, between the measured magnitudes for each of IPHAS fields 2540 and 2540o. The lower two panels show the colour rms deviations. The bin size is 0.5 mag for all but the i' data, where a binning of 0.25 mag was more convenient. See further discussion of fields 2540/2540o in Section 5. These data were obtained on a photometric night in 2003 November. The r' exposure times were 10 s in this case.

moon was setting. Calculated empirically as $\sqrt{\langle(m_{2540} - m_{2540o})^2\rangle}$ or its colour equivalent, over a range in mean magnitude $\Delta m = 0.5$ or $\Delta m = 0.25$, the error is corrected back to a representative single field measurement error by dividing by $\sqrt{2}$. The bright-end errors in the magnitudes themselves, in plots such as these, are typically dominated by calibration offsets of a few hundredths that will be removed when a final uniform survey calibration is devised. In the case of fields 2540 and 2540o, the offsets were all small (less than ~ 0.01). From 2004 onwards, when the r' exposures were increased to 30 s, the faint-end r' errors drop to around 60 per cent of those for 2003 (for the same sky conditions). This carries through to the colour errors falling to 80 per cent or less of their 2003 levels. Altogether, this significantly raises the fraction of catalogued objects that will meet the quality target of $\Delta r' \leq 0.1$ for $r' \leq 20$.

To date roughly 3 Tbyte of raw data from the first two seasons of IPHAS observing have been processed this way. This corresponds to well over 100 000 $4k \times 2k$ CCD images and over 40 million objects have been catalogued. All of this processed data is also available at the individual frame and catalogue level via a POSTGRESQL data base interface, which allows users to: postage stamp browse for candidate verification; construct image catalogue overlays, including on-the-fly matching with other catalogues such as the 2MASS point-source catalogue; perform on-demand continuum image subtraction and mosaicking of larger areas; access all the quality control information; and more (see Irwin et al. 2005). The data base interface is available on the Cambridge Astronomical Survey Unit (CASU) website (<http://apm2.ast.cam.ac.uk/cgi-bin/wfs/dqc.cgi>). Coordinates of the centres of the observed IPHAS fields are obtainable there.²

3 SIMULATION OF THE IPHAS COLOUR–COLOUR PLANE

The three bandpasses of the survey provide the basis for the construction of a number of magnitude–colour diagrams and a colour–colour diagram to describe any chosen region in the northern Galactic plane. Using just the two r' , i' , broad bandpasses, one may derive colour–magnitude diagrams that can in principle reveal different sequences at different reddenings that may be present in the field under investigation.

Full exploitation of IPHAS hinges on the colour–colour plane involving all three bands. The combination of magnitudes we use is $(r' - i')$ as abscissa and $(r' - H\alpha)$ as ordinate, so that objects with H α -band excesses appear higher within the diagram, while intrinsically redder or more highly reddened objects are over to the right. The most straightforward use that can be made of such diagrams is to pick out for spectroscopic follow-up those objects whose $(r' - H\alpha)$ colour places them clearly above the main locus of non-emission-line objects. Additional information contained within the colour–colour diagrams can lead to identification of more subtle candidate emission-line stars and also to a characterization of the stellar populations distributed along the line of sight. In this second sense, IPHAS can also be seen as providing a far-red map of stellar populations in the northern Galactic plane.

Fig. 3 is a composite $(r' - H\alpha, r' - i')$ plot derived from data obtained in three paired IPHAS fields (fields 4090/4090o, 4095/4095o and 4199/4199o: see Table 1). In each case, catalogues of sources

² These are identified via object names taking the form `intphas_nnnn *`, where `nnnn` is a four-digit number up to 7635 and `*` is the wild card for further characters identifying exposure type.

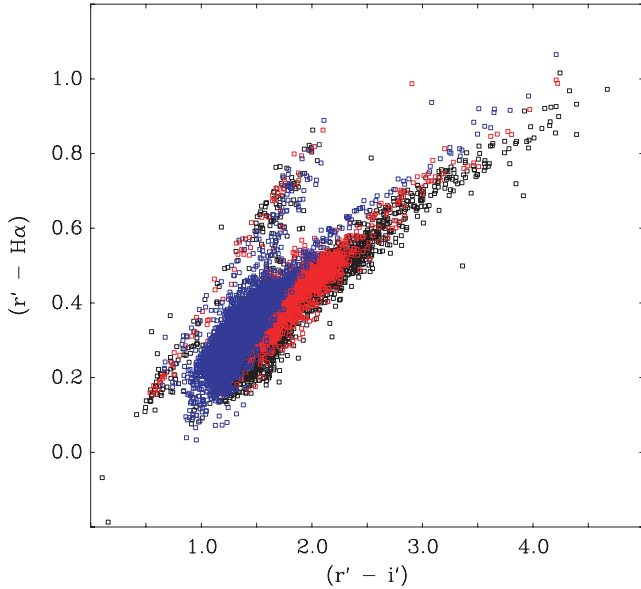


Figure 3. A plot of $(r' - H\alpha)$ versus $(r' - i')$ for 13 818 point sources extracted from the overlap area of the paired exposures for IPHAS fields 4199 (black points), 4090 (red points) and 4095 (blue points), in Aquila. The sources lie in the magnitude range $13 < r' < 20$. The colours for each object have been formed independently from each set of $H\alpha$, r' and i' exposures, and then averaged. The median error in either colour is ~ 0.03 at r' close to 19 and only occasionally exceeds 0.06 at the $r' = 20$ limit of the plot. Note the very well defined upper edge of the upper sequence: this is where unreddened main-sequence stars are located. The few stars above it are candidate emission-line objects.

classified by the CASU pipeline as either ‘definitely stellar’ or ‘probably stellar’ were extracted from within a 30×30 arcmin² box spanning most of the overlap region between the two pointings. For each extracted object, the datum plotted is the mean of the colours derived independently from each of the two exposures making up the field pair. The data shown are limited to the magnitude range $13 < r' < 20$, where the error in either colour is kept to less than ~ 0.05 mag. These are representative of the better data in the IPHAS data base in that they were obtained on photometric nights in 2004 June at times of ~ 1 -arcsec seeing and low sky background.

All three fields are located in the Aquila Rift region and sample sightlines that pass through the outer parts of the molecular cloud. Dame & Thaddeus (1985) noted that this is a nearby (~ 200 pc) and not particularly opaque cloud system, presenting around 2 mag of visual extinction only. This is a modest addition to the reddening through the remaining Galaxy beyond: the reddening data of Schlegel, Finkbeiner & Davis (1998) indicate maximum visual extinctions, A_V ranging from ~ 5 , in 4095, up to ~ 10 , in 4199. The nearby rift cloud is responsible for the lightly populated gap, seen in Fig. 3, between the upper sequence and the lower, but much more densely populated strip. The existence of this separation allows a clear demonstration of how well theoretically synthesized tracks compare with and make sense of the photometry.

To achieve an understanding of the behaviours seen in the colour-colour domain, we have constructed two types of synthetic tracks: the first type concerns the properties of normal stars without $H\alpha$ emission, while the second explores the impact of adding narrow $H\alpha$ emission to generic stellar spectral energy distributions (SEDs). We present these tracks below, using the Aquila fields to illustrate the former in Section 4.

3.1 The IPHAS colours of normal stars

For simulating the $(r' - H\alpha)$ and $(r' - i')$ colours of normal stars, we have used the library of stellar SEDs due to Pickles (1998, hereafter P98). At a final binning of 5 \AA the spectra in this library are well enough sampled that we may use them to compute narrow-band $H\alpha$ relative magnitudes with confidence, alongside the analogous broad-band r' and i' quantities. The required numerical filter transmission profiles, shown in Fig. 1, are available via the Isaac Newton Group (ING) WFC web pages (<http://www.ing.iac.es/Astronomy/instruments/wfc/>), as is a mean WFC CCD response curve. To ensure compliance with the Vega-based zero magnitude scale, we have defined synthetic colour as follows:

$$(r' - i') = -2.5 \log \left(\frac{\sum T_{r'} F_{\lambda} \Delta\lambda}{\sum T_{r'} F_{\lambda, V} \Delta\lambda} \right) + 2.5 \log \left(\frac{\sum T_{i'} F_{\lambda} \Delta\lambda}{\sum T_{i'} F_{\lambda, V} \Delta\lambda} \right), \quad (1)$$

where $T_{r'}$ and $T_{i'}$ are the r' and i' numerical transmission profiles, after multiplying by the mean WFC CCD response curve and re-binning to match the P98 spectral library sampling. The spectral energy distribution (SED) for Vega, $F_{\lambda, V}$, is the appropriately re-sampled version of that due to Hayes (1985). The $(r' - H\alpha)$ colour is evaluated in the same way, after substituting the $H\alpha$ numerical profile in place of the i' profile. Because Vega is an A0 V star, its SED at $H\alpha$ incorporates a strong absorption line feature. Currently, because the CASU pipeline uses broad-band standard fields to calibrate measured source magnitudes, there is an offset in $(r' - H\alpha)$ colour between the catalogue data and our simulations. The dominant spectral type in the standard fields will be appreciably later than the A0 of Vega, with the consequence that the standard-star SEDs will both be redder and less eroded by $H\alpha$ line absorption. On this basis, one would expect and we do find that zero $(r' - H\alpha)$ for unreddened main-sequence stars corresponds to $(r' - i') \sim 0.3$ (late F), rather than to $(r' - i') = 0$ (Vega, A0 V), in plots of IPHAS data obtained in photometric conditions. Hence, on comparing simulated tracks with observation it is necessary to correct for this. The best way to do this is to assume that only a shift in $(r' - H\alpha)$ is required, given that the calibration of the broad-band-only $(r' - i')$ colour should be secure enough (see Section 5 and the discussion of Fig. 9). The shift that needs to be applied to theoretical $(r' - H\alpha)$ values to match them to observation is then always downwards, varying in amount between about -0.10 and -0.25 .

We have simulated tracks for main-sequence stars (luminosity class V), giant stars (class III) and supergiants (class I) using, for simplicity only, solar metallicity P98 spectra. Each sequence has been calculated for a range of reddenings using an $R = 3.1$ optical-infrared (IR) extinction law in the form given by Howarth (1983). The colours derived are given for $E(B-V) = 0, 1, 2, 3$ and 4 in Tables 2 and 3. They are specified at this level of detail because there is no single reddening vector that translates all of a sequence directly on to its reddened counterpart. The unreddened dwarf, giant and supergiant sequences are compared in Fig. 4, where it can be seen that there is a gradual decrease in track gradient with increasing luminosity class. Nevertheless, between mid-F and late-K spectral types there is minimal distinction between the luminosity classes: this is the regime where $H\alpha$ absorption is weak and there is not yet any marked development of the molecular band structure that typifies M-type stars.

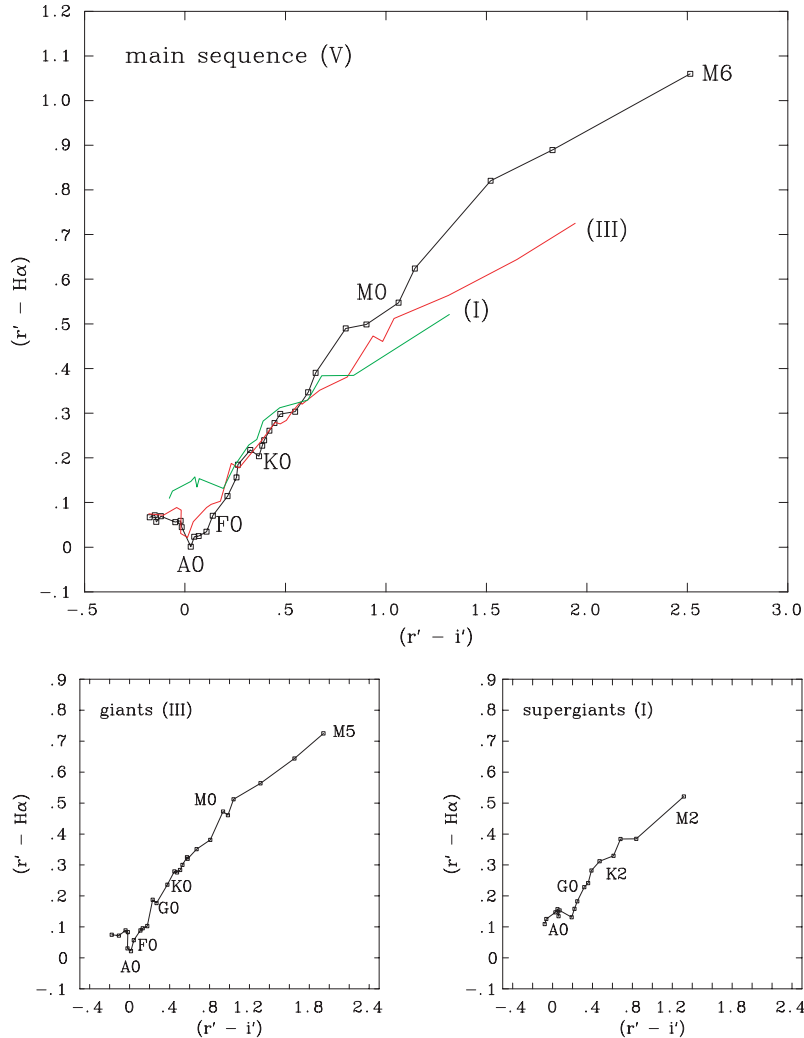
The effect of interstellar extinction on the sequences is illustrated in Fig. 5. With increasing reddening, the range of

Table 2. Synthetic tracks in the ($r' - H\alpha, r' - i'$) plane, for main-sequence dwarfs and giants, calculated for a range of reddenings.

Spectral type	Reddening									
	$E(B - V) = 0.0$		$E(B - V) = 1.0$		$E(B - V) = 2.0$		$E(B - V) = 3.0$		$E(B - V) = 4.0$	
	$(r' - i')$	$(r' - H\alpha)$								
O5 V	-0.176	0.067	0.493	0.274	1.146	0.438	1.784	0.560	2.408	0.643
O9 V	-0.151	0.072	0.519	0.278	1.173	0.441	1.811	0.563	2.436	0.645
B0 V	-0.143	0.057	0.529	0.264	1.184	0.427	1.824	0.549	2.451	0.632
B1 V	-0.120	0.069	0.552	0.273	1.209	0.435	1.850	0.554	2.478	0.635
B3 V	-0.049	0.056	0.623	0.258	1.279	0.418	1.919	0.535	2.546	0.614
B8 V	-0.022	0.059	0.649	0.259	1.304	0.416	1.944	0.532	2.572	0.609
B9 V	-0.016	0.045	0.652	0.243	1.305	0.399	1.943	0.514	2.569	0.590
A0 V	0.029	0.001	0.699	0.199	1.352	0.355	1.991	0.468	2.616	0.544
A2 V	0.046	0.023	0.716	0.220	1.370	0.374	2.009	0.486	2.634	0.560
A3 V	0.068	0.025	0.737	0.220	1.391	0.372	2.029	0.483	2.654	0.555
A5 V	0.107	0.035	0.776	0.228	1.428	0.379	2.065	0.488	2.689	0.558
A7 V	0.138	0.070	0.805	0.261	1.457	0.408	2.094	0.515	2.717	0.584
F0 V	0.212	0.114	0.876	0.299	1.525	0.441	2.159	0.542	2.780	0.606
F2 V	0.257	0.156	0.920	0.338	1.567	0.477	2.201	0.576	2.822	0.638
F5 V	0.263	0.185	0.926	0.364	1.574	0.502	2.208	0.600	2.830	0.661
F8 V	0.325	0.218	0.985	0.393	1.631	0.526	2.262	0.620	2.882	0.677
G0 V	0.368	0.204	1.028	0.378	1.673	0.510	2.303	0.602	2.921	0.658
G2 V	0.384	0.227	1.043	0.400	1.687	0.530	2.317	0.621	2.935	0.676
G5 V	0.394	0.239	1.052	0.411	1.695	0.540	2.323	0.630	2.941	0.684
G8 V	0.420	0.261	1.077	0.429	1.718	0.556	2.345	0.643	2.961	0.695
K0 V	0.445	0.278	1.098	0.443	1.736	0.567	2.360	0.651	2.973	0.700
K2 V	0.474	0.298	1.127	0.461	1.765	0.582	2.390	0.665	3.004	0.713
K3 V	0.548	0.303	1.199	0.463	1.836	0.581	2.460	0.660	3.073	0.705
K4 V	0.613	0.347	1.262	0.502	1.895	0.615	2.515	0.691	3.126	0.732
K5 V	0.650	0.390	1.301	0.544	1.937	0.658	2.561	0.735	3.175	0.778
K7 V	0.800	0.490	1.450	0.636	2.085	0.743	2.709	0.812	3.322	0.849
M0 V	0.903	0.499	1.553	0.641	2.188	0.743	2.811	0.807	3.424	0.839
M1 V	1.063	0.547	1.719	0.688	2.360	0.789	2.987	0.853	3.604	0.885
M2 V	1.144	0.624	1.795	0.756	2.431	0.849	3.055	0.907	3.669	0.934
M3 V	1.521	0.820	2.174	0.941	2.811	1.023	3.436	1.070	4.052	1.088
M4 V	1.829	0.889	2.470	0.995	3.096	1.061	3.710	1.095	4.315	1.099
M6 V	2.514	1.060	3.165	1.143	3.801	1.191	4.425	1.207	5.041	1.198
O8 III	-0.180	0.075	0.489	0.282	1.142	0.446	1.780	0.568	2.404	0.651
B1-2 III	-0.108	0.072	0.565	0.276	1.222	0.438	1.863	0.558	2.491	0.639
B3 III	-0.042	0.089	0.630	0.291	1.285	0.449	1.925	0.566	2.551	0.644
B5 III	-0.019	0.083	0.653	0.283	1.308	0.441	1.947	0.557	2.573	0.634
B9 III	-0.022	0.031	0.649	0.231	1.303	0.388	1.942	0.504	2.568	0.582
A0 III	0.013	0.022	0.682	0.220	1.335	0.375	1.973	0.489	2.598	0.565
A3 III	0.041	0.057	0.708	0.252	1.358	0.404	1.994	0.515	2.617	0.587
A5 III	0.107	0.089	0.772	0.280	1.420	0.429	2.053	0.537	2.674	0.606
A7 III	0.130	0.096	0.797	0.285	1.447	0.432	2.083	0.539	2.706	0.607
F0 III	0.177	0.103	0.844	0.290	1.497	0.435	2.134	0.539	2.759	0.606
F2 III	0.230	0.188	0.890	0.368	1.534	0.506	2.164	0.603	2.782	0.664
F5 III	0.269	0.177	0.930	0.356	1.575	0.492	2.206	0.588	2.825	0.648
G0 III	0.378	0.236	1.035	0.408	1.677	0.537	2.306	0.627	2.923	0.681
G5 III	0.449	0.279	1.102	0.444	1.739	0.567	2.364	0.651	2.977	0.700
G8 III	0.474	0.276	1.128	0.440	1.767	0.563	2.392	0.647	3.007	0.696
K0 III	0.505	0.284	1.157	0.445	1.793	0.564	2.417	0.646	3.029	0.692
K1 III	0.529	0.300	1.182	0.461	1.820	0.580	2.445	0.660	3.059	0.706
K2 III	0.574	0.325	1.225	0.481	1.860	0.596	2.483	0.673	3.095	0.716
K3 III	0.582	0.320	1.230	0.475	1.863	0.589	2.483	0.665	3.092	0.706
K4 III	0.670	0.351	1.320	0.502	1.955	0.611	2.578	0.683	3.191	0.721
K5 III	0.808	0.381	1.456	0.525	2.088	0.629	2.708	0.695	3.318	0.728
M0 III	0.935	0.473	1.581	0.611	2.212	0.708	2.830	0.768	3.438	0.796
M1 III	0.984	0.461	1.633	0.598	2.266	0.695	2.887	0.755	3.496	0.782
M2 III	1.040	0.512	1.679	0.641	2.304	0.730	2.916	0.782	3.519	0.803
M3 III	1.311	0.564	1.957	0.687	2.586	0.770	3.203	0.817	3.809	0.832
M4 III	1.652	0.644	2.296	0.753	2.924	0.822	3.539	0.857	4.144	0.860
M5 III	1.941	0.725	2.581	0.821	3.205	0.879	3.816	0.904	4.417	0.899

Table 3. Synthetic tracks in the $(r' - H\alpha, r' - i')$ plane for supergiant stars calculated for a range of reddenings.

Spectral type	Reddening									
	$E(B - V) = 0.0$		$E(B - V) = 1.0$		$E(B - V) = 2.0$		$E(B - V) = 3.0$		$E(B - V) = 4.0$	
	$(r' - i')$	$(r' - H\alpha)$								
B0I	-0.078	0.109	0.591	0.311	1.243	0.470	1.880	0.588	2.504	0.666
B3I	-0.063	0.126	0.603	0.325	1.253	0.481	1.888	0.596	2.510	0.672
B5I	0.029	0.147	0.693	0.341	1.340	0.491	1.973	0.601	2.594	0.672
B8I	0.049	0.157	0.717	0.351	1.369	0.502	2.007	0.612	2.631	0.683
A0I	0.060	0.135	0.726	0.327	1.377	0.477	2.012	0.586	2.636	0.657
A2I	0.071	0.154	0.734	0.345	1.382	0.493	2.015	0.601	2.636	0.671
F0I	0.191	0.131	0.856	0.318	1.505	0.462	2.140	0.565	2.762	0.631
F5I	0.219	0.158	0.882	0.340	1.529	0.480	2.162	0.580	2.783	0.643
F8I	0.248	0.183	0.908	0.363	1.553	0.500	2.184	0.597	2.803	0.657
G0I	0.317	0.229	0.971	0.401	1.609	0.531	2.234	0.622	2.847	0.677
G2I	0.357	0.241	1.010	0.412	1.648	0.540	2.272	0.629	2.885	0.682
G5I	0.389	0.282	1.040	0.449	1.676	0.573	2.298	0.658	2.909	0.708
G8I	0.471	0.312	1.109	0.468	1.731	0.584	2.340	0.661	2.940	0.704
K2I	0.611	0.329	1.251	0.481	1.876	0.591	2.488	0.663	3.089	0.701
K3I	0.680	0.384	1.316	0.528	1.935	0.632	2.543	0.699	3.140	0.733
K4I	0.839	0.385	1.485	0.526	2.115	0.626	2.733	0.689	3.340	0.719
M2I	1.316	0.521	1.956	0.642	2.580	0.723	3.193	0.769	3.795	0.784

**Figure 4.** The expected positions of unreddened main-sequence (top), giant (bottom left) and supergiant stars (bottom right) in the $(r' - H\alpha, r' - i')$ plane according to spectral type. In the top panel, the giant and supergiant tracks (respectively, red and green) are superimposed to show their positioning relative to the main sequence.

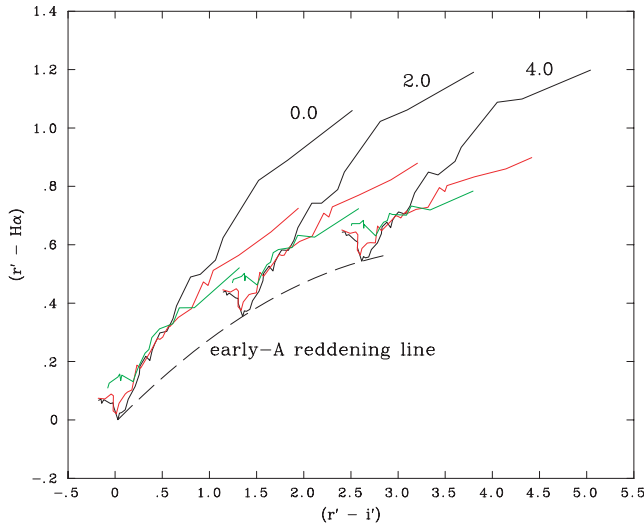


Figure 5. The effect of interstellar extinction, calculated according to an $R = 3.1$ Galactic law, on synthetic stellar tracks in the $(r' - H\alpha, r' - i')$ plane. As in Fig. 4, the main sequences are drawn in black, the giant sequences in red and supergiants in green. The three sets shown apply to $E(B - V) = 0.0, 2.0$ and 4.0 , as labelled. The dashed line shown is the reddening locus for A0 V stars. This defines a notional minimum line for all non-degenerate stars. It is named the ‘early A reddening line’ for reasons that become clear in Section 5.

$(r' - H\alpha)$ colour spanned by each luminosity-class sequence diminishes. This shrinkage in dynamic range is due to effective wavelength of the r' bandpass lengthening and moving closer to the $H\alpha$ bandpass as reddening becomes ever more extreme. It may be seen in Fig. 5 that the supergiant sequence essentially reddens along itself, while the main and giant sequences shift across in a manner that sweeps out area in the colour–colour plane. Also shown in this figure is the reddening locus for A0 dwarfs: for non-degenerate stars and binaries, this line amounts to an important boundary in that none should drop below it. In practice, stars will be carried into the forbidden domain by a range of types of observational error. Degenerate dwarfs and related objects with stronger $H\alpha$ absorption than early A stars would also fall below this line.

3.2 The IPHAS colours of emission-line stars

To assess the impact on $(r' - H\alpha)$ and $(r' - i')$ colours of increasingly strong $H\alpha$ emission, we have represented underlying stellar SEDs using simple power laws or, at later spectral types, blackbodies. At the acceptable price of some approximation, such as ignoring stronger spectral features like the Paschen limit, this approach allows us to explore a broad range of SEDs flexibly and to quantify thresholds for the straightforward detection of $H\alpha$ emission. We present results for four simple SEDs: three power laws of the form $F_\lambda \propto \lambda^{-\beta}$ with β set equal to 4 (Rayleigh–Jeans case, relevant to the hottest O stars), 3 (appropriate to \sim A0 stars) and 2.3 (the optically thick accretion disc case); a Planck function at a temperature of 5900 K that is a good match to the G2 V SED in the P98 library.

$H\alpha$ emission, where present, takes on a wide range of profiles in stellar spectra and can be practically any width: with FWHM anywhere in the range from a few tens of km s^{-1} up to thousands. However, for now, we treat the simple limiting case of $H\alpha$ emission that is well-contained within the width of the INT/WFC narrow-band $H\alpha$ filter. The particular realization used is of a rectangular profile of breadth 25 \AA centred at 6570 \AA (note that the effective $H\alpha$ filter

bandpass is blueshifted for objects observed off-axis, which is why the central wavelength of the WFC filter is accordingly specified as 6568 \AA). This yields results negligibly different from using a Gaussian profile.

The synthesis of colours consists of the following steps: an underlying stellar SED is chosen; a rectangular $H\alpha$ emission profile of the desired equivalent width (EW) is superimposed; the resultant artificial spectrum is then reddened as required using the reddening law specified in Section 3.1; finally, the reddened SED is multiplied by the product of the survey filter profiles and WFC response and integrated to form colours as in equation (1). We have not attempted to apply this procedure to very late type SEDs dominated by molecular bands: in these stars, neither can the SED be easily parametrized, nor is an objective definition of the $H\alpha$ EW straightforward.

On the basis of this procedure, we have synthesized colours for the same set of reddenings [$E(B - V) = 0$ to 4 in steps of 1] for each of the 4 adopted stellar SEDs. Our results are presented in Fig. 6 and in Table 4. We find that there is a practical degeneracy between reddening and underlying SED such that a very-nearly unique locus is traced at each adopted $H\alpha$ emission EW. This means that, in principle, a given location in the colour–colour plane, above the main stellar locus, is associated with a particular $H\alpha$ EW.

A further property of the SED-specified tracks is that at an EW of up to $\sim 100 \text{ \AA}$, the trend with increasing EW is nearly vertical. However, as the $H\alpha$ EW becomes very large, the tracks bend towards smaller $(r' - i')$ as the $H\alpha$ emission becomes a more significant contributor to the r' flux. Indeed beyond an EW of 1000 \AA as the switch from a ‘stellar’ to a ‘nebular’ spectrum with little discernable continuum takes place, the bending becomes very extreme. In reality, $(r' - i')$ in the nebular case will also depend somewhat on the relative strength of line emission in the i' band: left out of consideration here. The limiting value of $(r' - H\alpha)$ in the absence of any continuum is ~ 3.24 for our synthetic system referred to the Hayes (1985) SED for Vega (see Table 4). At the present time, without a properly defined zero-point to the $H\alpha$ filter magnitudes, this translates to an effective observed upper limit on $(r' - H\alpha)$ of around 3.1: any value appreciably above this signals a problem with the photometry of the individual object.

Finally, an important feature to note in the trend in IPHAS colours with respect to both the emission EW and reddening is that the threshold for the detection of $H\alpha$ emission is lowest for bluer and/or less reddened objects (see Fig. 6). This implies, for instance, that IPHAS will pick out faint, nearby accreting objects very well indeed down to just a few angstroms EW. Conversely, in the worst case of a densely populated main stellar locus spanning a wide range of reddenings, the EW threshold on the straightforward detection of classical T Tau stars at $E(B - V) \sim 2$ ($A_V \sim 6$) is around 30 \AA . Not infrequently, however, at larger $(r' - i')$ ($\gtrsim 2$), the colour–colour plane below the unreddened main sequence may be sparsely populated: the few objects located here could be the result of a combination of anomalous reddening and line emission. Indeed, it is generally the case that objects, checked as having reliable photometry, lying outside the bounds of the densely populated main stellar locus for their field, have a relatively high probability of being interesting in one way or another.

4 SIMULATED AND OBSERVED IPHAS COLOUR–COLOUR DIAGRAMS COMPARED: FIELDS IN AQUILA

With the assistance of the synthetic tracks derived in the preceding section, it is possible to begin to make sense of the morphologies

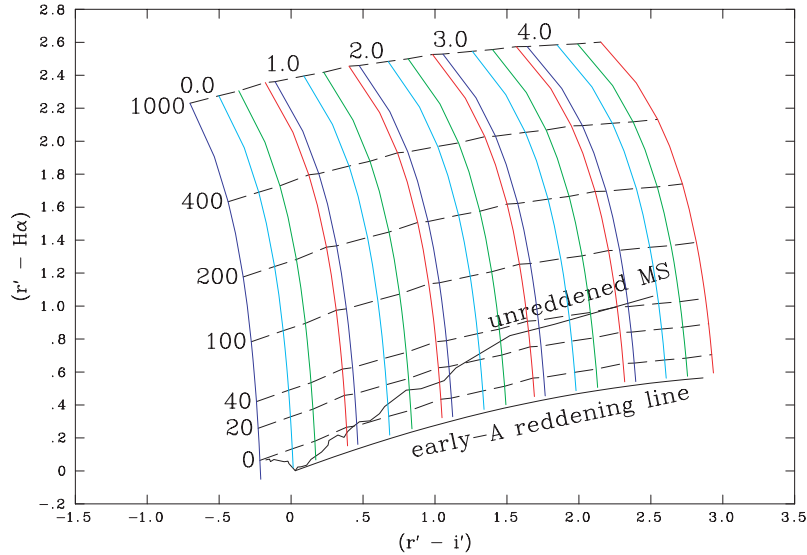


Figure 6. The effect of adding in increasing $H\alpha$ emission to a range of simplified stellar SEDs. The black lines, representing an unreddened main sequence and the early A reddening trend, are the expected bounds to the main stellar locus. The dashed lines are lines of the constant $H\alpha$ emission equivalent width, with the label at the left specifying the equivalent width in angstroms. The vertical coloured lines are, in effect, $H\alpha$ emission curves of growth for particular choices of underlying SED and reddening: the darker blue lines are for the Rayleigh–Jeans case ($F_\lambda \propto \lambda^{-4}$) at different reddenings; light blue and green lines are for power-law indices of -3 and -2.3 respectively, while the red lines are the results for a 5900-K blackbody (a G2 V star, roughly). The lowest point on each curve corresponds to a narrow net $H\alpha$ absorption of EW, 10 Å. The reddenings, as $E(B - V)$, are specified across the top and refer to each set of coloured lines.

appearing in IPHAS ($r' - H\alpha$, $r' - i'$) diagrams: with a view to their fuller exploitation. For this purpose, we have selected some of the highest quality IPHAS observations obtained from pointings in the Aquila Rift region, allowing us to exploit its distinctive and easily interpreted colour–colour domain morphologies.

We begin with field 4095 in Aquila, included in Fig. 3 as the blue data points. This field is roughly centred on $\ell = 32.5^\circ$, $b = +4.8^\circ$, sampling a region close to the Galactic latitude upper limit of the survey. The reddening data of Schlegel et al. (1998) indicates that $E(B - V)$ typically does not exceed 1.6 in this direction. This makes it the least obscured of the three fields and, correspondingly, the field presenting the highest apparent density of stars (7097 out of the 13 818 in Fig. 3). In Fig. 7, the data on extracted point sources are compared with selected synthetic tracks that have all been shifted downwards in $(r' - H\alpha)$ by 0.17 to best match them to the data.

The upper panel in Fig. 7 shows the brighter end of the magnitude range ($13 < r' < 18$) that includes a modest number of very nearly unreddened M dwarfs and a much larger number of mainly giant stars. Indeed, the M giants form a particularly tight sequence at $(r' - i') \gtrsim 2.0$. This suggests that most of the Galactic reddening along this sight line accumulates nearby because, if it did not, we would expect to see a more smeared giant distribution. The simulated giant tracks for $E(B - V) = 1.4$ and 1.6 are compared with this very well-defined feature. For $(r' - i') \lesssim 2$, many of the brighter objects will be giants at a plausible reddening; however, at $(r' - i') > 2$, the synthesized tracks for M2–5 III stars fall too low by ~ 0.05 in $(r' - H\alpha)$. A similar problem affects comparisons between synthesized and observed tracks for M dwarfs also (see below). At $r' < 18$, only one object falls significantly below the early A reddening line: it is likely to be a white dwarf or related object.

The lower panel in Fig. 7 presents the faint end of the r' magnitude range, with the synthetic main sequence and giant tracks, reddened to $E(B - V) = 1.6$, superimposed. The main locus of observed objects is now a little more steeply angled, indicating that these

fainter stars include a much increased component of main-sequence objects. However, at $r' \simeq 20$, stars later in spectral type than mid-K are only detectable at $E(B - V) \lesssim 0.8$, as evidenced by the scatter of points extending the main stellar locus up to $(r' - H\alpha) \sim 0.9$. The small proportion of the plotted objects falling below the early A reddening line can be presumed consistent with observational error. The 0.17 offset of the synthesized tracks was determined by optimizing the positioning of both this notional line and the unreddened main sequence with respect to the data for $r' \leq 18$. These particular IPHAS observations have captured objects out to the limits of the Galactic disc population, such as reddened mid-M giants at ~ 10 kpc, located around 800 pc above the mid-plane at about the location of the far Sagittarius–Carina arm.

The more highly reddened Aquila field 4199, centred at $\ell = 34.3^\circ$, $b = +1.8^\circ$, provides some degree of contrast with 4095 and is illustrated in Fig. 8. The reddening here is more variable with position, as well as more extreme. This shows itself directly in the broader red giant locus. Superimposed on the colour–colour plot are synthesized giant-star tracks for $E(B - V) = 2.4$ and 3.0 . The latter value was selected because the maximum Galactic extinction for this field, derived from the Schlegel et al. 1998 mapping data, is $E(B - V) \simeq 3.0$. There is a rough consistency here with the findings from field 4095, in that the M giant track synthesized for this extinction falls a bit below the observed thinning of putative M giants (as it did for field 4095). Down to $r = 20$, the colour–colour data suggest the presence of main-sequence stars of K and earlier type at reddenings in the range $1.2 \lesssim E(B - V) \lesssim 2.4$: the main-sequence tracks for these limits are drawn to illustrate this (Fig. 8). This field again bears the imprint of the Aquila Rift in the relative deficit of stars between the lightly populated zero-extinction main sequence and the dense locus of stars at $E(B - V) \gtrsim 1.2$.

In field 4199, it is more apparent that the observed unreddened M dwarfs tend to maintain the locus gradient defined at earlier spectral types, rather than begin to turn over as the synthesized track

Table 4. Synthetic tracks in the ($r' - H\alpha, r' - i'$) plane, for increasing $H\alpha$ emission equivalent width. Data are provided for four underlying simplified stellar SEDs (three power laws and a blackbody) and for a range of reddenings. The usual sign convention for the $H\alpha$ EW (left hand column) is reversed in that positive values refer to net emission.

H α EW (\AA)	Reddening									
	$E(B - V) = 0.0$		$E(B - V) = 1.0$		$E(B - V) = 2.0$		$E(B - V) = 3.0$		$E(B - V) = 4.0$	
	$(r' - i')$	$(r' - H\alpha)$								
1. $F_\lambda \propto \lambda^{-4}$ (Rayleigh-Jeans)										
0	-0.217	0.064	0.456	0.274	1.114	0.441	1.756	0.567	2.385	0.654
10	-0.223	0.166	0.449	0.375	1.105	0.542	1.746	0.666	2.374	0.752
20	-0.229	0.259	0.442	0.467	1.097	0.632	1.737	0.756	2.364	0.841
40	-0.241	0.421	0.427	0.626	1.080	0.789	1.718	0.911	2.343	0.995
60	-0.253	0.559	0.413	0.762	1.063	0.923	1.699	1.043	2.323	1.125
80	-0.265	0.679	0.399	0.880	1.047	1.038	1.681	1.156	2.303	1.237
100	-0.277	0.784	0.385	0.983	1.030	1.140	1.663	1.256	2.284	1.335
150	-0.305	1.004	0.350	1.197	0.991	1.348	1.619	1.460	2.237	1.536
200	-0.333	1.177	0.317	1.365	0.953	1.512	1.577	1.620	2.192	1.693
300	-0.386	1.441	0.254	1.619	0.881	1.756	1.497	1.857	2.107	1.925
400	-0.438	1.635	0.194	1.804	0.813	1.934	1.423	2.028	2.028	2.092
1000	-0.702	2.232	-0.109	2.363	0.477	2.460	1.061	2.528	1.647	2.573
1 000 000	-7.094	3.241	-6.632	3.241	-6.143	3.242	-5.627	3.242	-5.086	3.242
2. $F_\lambda \propto \lambda^{-3}$ (\sim A0 SED)										
0	0.008	0.134	0.677	0.331	1.331	0.485	1.970	0.598	2.596	0.673
10	0.001	0.236	0.670	0.432	1.322	0.585	1.960	0.697	2.586	0.771
20	-0.005	0.328	0.662	0.523	1.313	0.675	1.950	0.786	2.575	0.860
40	-0.018	0.490	0.647	0.682	1.296	0.832	1.931	0.941	2.554	1.013
60	-0.031	0.627	0.632	0.817	1.278	0.964	1.912	1.072	2.534	1.143
80	-0.043	0.746	0.617	0.934	1.261	1.079	1.893	1.185	2.514	1.255
100	-0.056	0.851	0.602	1.036	1.245	1.180	1.874	1.284	2.494	1.353
150	-0.086	1.069	0.566	1.248	1.204	1.387	1.829	1.487	2.446	1.553
200	-0.115	1.241	0.531	1.415	1.164	1.549	1.786	1.646	2.400	1.709
300	-0.172	1.501	0.465	1.666	1.090	1.792	1.705	1.882	2.314	1.940
400	-0.226	1.692	0.403	1.849	1.020	1.967	1.629	2.051	2.234	2.105
1000	-0.503	2.277	0.088	2.396	0.674	2.484	1.260	2.544	1.849	2.583
1 000 000	-6.940	3.241	-6.468	3.242	-5.969	3.242	-5.444	3.242	-4.893	3.242
3. $F_\lambda \propto \lambda^{-2.3}$ (optically thick disc accretion)										
0	0.165	0.181	0.832	0.368	1.483	0.513	2.120	0.617	2.744	0.684
10	0.158	0.283	0.824	0.469	1.474	0.613	2.110	0.716	2.733	0.783
20	0.151	0.375	0.816	0.560	1.465	0.703	2.100	0.805	2.723	0.871
40	0.138	0.535	0.800	0.718	1.447	0.859	2.080	0.960	2.702	1.024
60	0.125	0.672	0.784	0.853	1.429	0.991	2.060	1.090	2.681	1.154
80	0.112	0.791	0.769	0.969	1.411	1.106	2.041	1.203	2.661	1.265
100	0.099	0.895	0.754	1.071	1.394	1.206	2.022	1.302	2.641	1.363
150	0.067	1.112	0.717	1.282	1.352	1.412	1.977	1.504	2.593	1.563
200	0.037	1.283	0.681	1.448	1.312	1.574	1.933	1.662	2.546	1.719
300	-0.022	1.541	0.613	1.697	1.236	1.814	1.850	1.897	2.459	1.949
400	-0.078	1.730	0.548	1.878	1.164	1.988	1.773	2.065	2.379	2.114
1000	-0.364	2.306	0.227	2.418	0.813	2.499	1.401	2.554	1.992	2.589
1 000 000	-6.830	3.241	-6.351	3.242	-5.846	3.242	-5.314	3.242	-4.757	3.242
4. 5900-K blackbody (\sim G2 V SED)										
0	0.385	0.265	1.040	0.435	1.681	0.563	2.308	0.652	2.924	0.705
10	0.377	0.367	1.032	0.535	1.671	0.662	2.297	0.750	2.913	0.803
20	0.370	0.458	1.023	0.625	1.662	0.752	2.287	0.839	2.902	0.891
40	0.356	0.618	1.006	0.783	1.643	0.907	2.266	0.993	2.880	1.044
60	0.341	0.753	0.990	0.916	1.624	1.039	2.246	1.123	2.859	1.173
80	0.327	0.871	0.974	1.032	1.606	1.152	2.227	1.235	2.839	1.285
100	0.314	0.975	0.957	1.133	1.588	1.252	2.207	1.333	2.818	1.382
150	0.280	1.189	0.918	1.342	1.544	1.456	2.160	1.535	2.769	1.581
200	0.247	1.357	0.880	1.506	1.502	1.616	2.115	1.691	2.722	1.736
300	0.184	1.611	0.808	1.751	1.423	1.854	2.030	1.924	2.634	1.965
400	0.124	1.797	0.741	1.929	1.349	2.025	1.952	2.090	2.552	2.128
1000	-0.177	2.358	0.406	2.456	0.988	2.526	1.571	2.572	2.161	2.599
1 000 000	-6.695	3.241	-6.210	3.242	-5.698	3.242	-5.161	3.242	-4.598	3.242

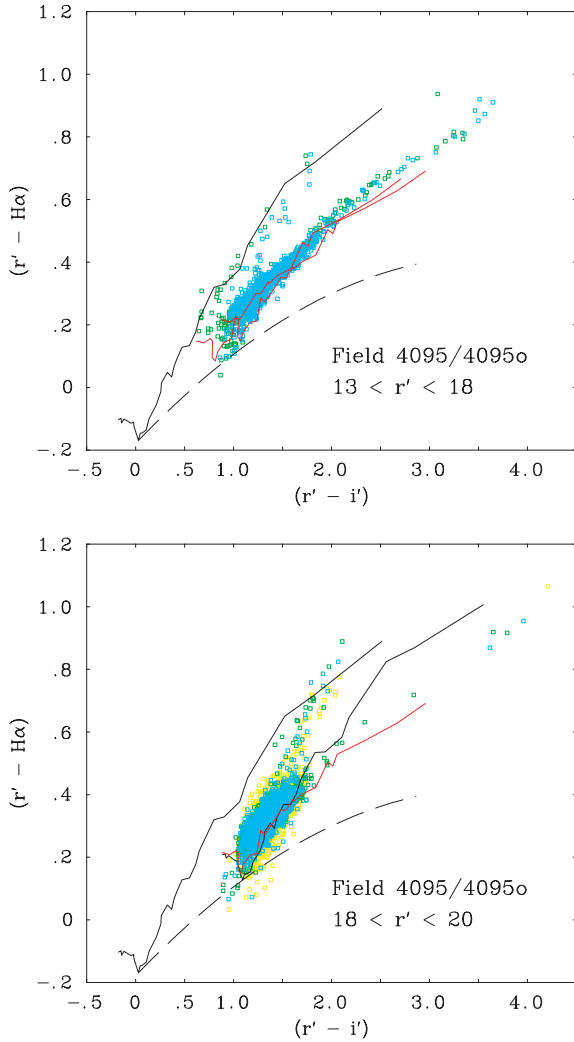


Figure 7. The $(r' - H\alpha, r' - i')$ plane derived from observations of IPHAS fields 4095/4095o, compared with selected synthetic tracks. In both panels, the uppermost solid line traces the unreddened main-sequence track, while the dashed line is the early A reddening line. See text for specification of other tracks. In the upper panel, green points indicate $r' < 16$, while blue indicates $r' > 16$. Below, yellow corresponds to $19.5 < r' < 20$, green to $19 < r' < 19.5$ and blue to $18 < r' < 19$.

indicates they should. This is most likely another symptom of the problem behind the M-giant discrepancy. At the present time, the available conversion between Landolt $(R - I)$ colours, appropriate to the standard star fields, and Sloan $(r' - i')$ are not properly defined for M dwarf colours (see Smith et al. 2002). Similarly, the existing conversion used in the CASU pipeline is not validated for $(r' - i') > 1.5$. Clearly, this will need to be corrected in the future. In the mean time, the comparison between observations of M stars and synthesized data will be increasingly qualitative as $(r' - i')$ increases beyond the validation limit.

In neither field 4095 nor field 4199 do supergiants stand out in any obvious morphological way. This is likely to be both a consequence of their relative rarity and of the way in which their locus shifts almost along itself with increasing reddening. In principle, extremely red, isolated objects located below the red giant locus could be picked out as candidate reddened supergiants: or as potential examples of other interesting object types. Indeed, we find that

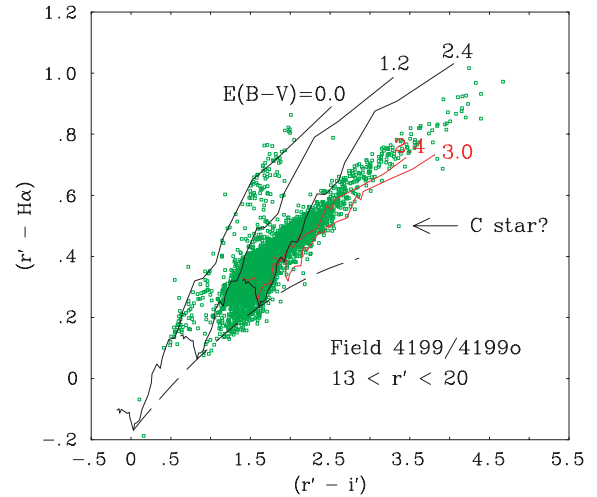


Figure 8. The $(r' - H\alpha, r' - i')$ plane derived from observations of IPHAS fields 4199/4199o, compared with selected synthetic tracks. The solid black lines are main-sequence tracks for $E(B - V) = 0$ and 2.4, while the dashed line is the early A reddening line. The two red tracks are giant tracks, for $E(B - V) = 2.4$ and 3.0. The position of the probable C star discussed in the text is picked out by the arrow.

IPHAS J184644.25+015324.6, the one isolated object in this part of the 4199 colour–colour plane at $(r' - i', r' - H\alpha) = (3.36 \pm 0.02, 0.499 \pm 0.03)$, cannot be a reddened supergiant. One reason is that the reddening [$E(B - V) \gtrsim 4$] required to explain its position in these terms is excessive relative to the maximum expected for the field. Another is that the 2MASS point source within 0.2 arcsec of the position of this object exhibits very bright JHK magnitudes with unusual colours [$K = 9.55 \pm 0.02$, $(J - H) = 1.68 \pm 0.03$, $(H - K) = 0.76 \pm 0.03$]. At $r' = 18.75 \pm 0.01$, there are no grounds for doubting the reliability of the IPHAS photometry and the reality of the source. The absence of any significant proper motion rules this object out as a nearby brown dwarf. This object is largely absent from pre-existing photographic surveys, except that there is a detection of it in the UKST Infrared (IVN-emulsion) Survey reported on the SuperCOSMOS Sky Survey website (<http://www-wfau.roe.ac.uk/sssf/>): it is reported there at an I magnitude of 18.383, around 3 mag fainter than the IPHAS i' magnitude. The IVN plate was obtained in 1981. This variability, the anomalously low $(r' - H\alpha)$ colour, together with its near-infrared (NIR) colours, point towards a carbon star at a reddening corresponding to $E(B - V) \sim 1.4$ (see e.g. Bessell & Brett 1988). A faint-end absolute K magnitude for such a star, if on the AGB, would be -6.5 (Claussen et al. 1987). This places it at ~ 15 kpc.

5 A COMPARISON BETWEEN FLUX-CALIBRATED SPECTRA AND IPHAS PHOTOMETRY: A FIELD IN TAURUS

Up to this point, the interpretation of the $(r' - H\alpha, r' - i')$ plane has been based on synthetic photometry derived from P98 library spectra. Early in 2004 February, we obtained William Herschel Telescope (WHT)/ISIS service spectra of six stars selected from IPHAS data on fields 2540 and 2540o in Taurus. These IPHAS images, obtained on 2003 November 5, were among the first to be pipeline processed and were picked for closer investigation as examples of apparently good quality data obtained in good seeing and photometric conditions. The aim of the follow-up service spectra was to

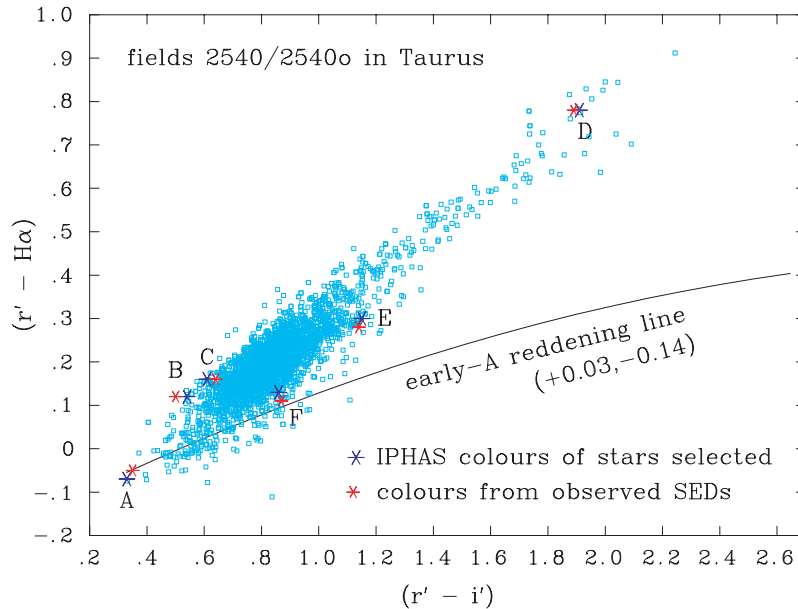


Figure 9. The $(r' - H\alpha, r' - i')$ diagram for IPHAS fields 2540 and 2540o, sampling an area roughly equivalent to 30×30 arcmin² around RA 05^h 33^m 40^s, Dec. +25° 20' 00" (J2000) in Taurus. The magnitude range shown is $13 \leq r' \leq 20$. The dark blue asterisks mark the colours of the six objects for which WHT/ISIS service spectra were obtained (stars A–F; see also Fig. 10 and Table 5). The red asterisks mark the ‘predicted’ colours derived from the flux-calibrated spectra, after applying the same shift to all six objects in order to minimize the mean difference with respect to the original IPHAS colours. Like the computed colours for stars A–F, the synthesized early A reddening line has been shifted by +0.03 and –0.14 in $(r' - i')$ and $(r' - H\alpha)$, respectively.

obtain relative spectrophotometry in order to ascertain optical SEDs, spectral types and reddenings for the sample stars as a retrospective check on the IPHAS colours and the typical errors in them. This exercise gives an impression both of the current state of the photometric calibration of the data and of the quality of the synthetic colour comparisons derived from P98.

Field 2540 is centred on RA 05^h 33^m 49^s, Dec. +25° 15' 00" (2000) in Taurus, only a few degrees from the Galactic anticentre direction. The characteristics of this sky position are very different from those in Aquila: here, the maximum Galactic reddening is modest and more smoothly varying, ranging from $E(B - V) \simeq 0.8$ in the NE of the $\sim 30 \times 30$ arcmin² extracted region up to ~ 1.1 in its SW. The other obvious difference, which stands out in the $(r' - H\alpha, r' - i')$ plot for 2540/2540o in Fig. 9, is the absence of any red giants within the magnitude range shown ($13 < r' < 20$). This absence is not just a consequence of the imposed magnitude limits because a K/M giant at 10 kpc viewed through approximately three visual magnitudes of extinction should be detected at $r' \sim 17$; it must be a real absence. In the example of solar and lower metallicity isochrones presented by Bertelli et al. (1994), a red giant branch is only well developed from around 100 million years of age onwards: suggesting that the stellar populations sampled in this part of the outer Galaxy are younger than this.

Eight stars were initially selected for ISIS spectroscopy from the colour–colour diagram for fields 2540/2540o, on the basis that they were not too faint ($r' < 18$) and lay on the outer boundary of the main stellar locus (dark blue asterisks in Fig. 9). These criteria biased the selection in favour of evolved spectral types. In the event, six of the eight stars (which we refer to as stars A–F) were observed during a service night of mediocre weather. Both the blue and red arms of ISIS were used, with the R600B and R316R gratings installed, delivering spectra spanning 3500–5000 and 6000–8700 Å for each star. To further the aim of relative spectrophotometry, the slit width was set fairly wide at 1.8 arcsec, while the slit orientation tracked

the parallactic angle. The resolution of the spectra is ~ 3.6 Å. An observation of the white dwarf G191–B2B was also obtained to serve as a spectrophotometric flux standard.

The data were extracted from the CCD frames and then wavelength and flux calibrated using routines from the software package, FIGARO. The extracted 1D spectra were then imported to the software tool, DIPSO, in order to determine approximate spectral types and reddenings by comparing them with P98 library spectra. In every case, the spectral type determination rested on matching absorption line characteristics. This matching was performed using the blue spectra for all but the M4 V star (star D): for this object, the red spectrum was more appropriate. For each star, the P98 library spectrum of the appropriate spectral type was progressively reddened, using the mean Galactic extinction law (Howarth 1983), to identify the best-fitting colour excess. The observed spectra and the best fits to them derived in this manner are shown in Fig. 10. The positions, magnitudes and further data on the six stars appear in Table 5. For star F, the data are not of sufficient quality to provide a reasonable fix on luminosity class: however, we suspect that its H α profile indicates a lower gravity than a main-sequence A5 star. The final step of deriving photometric colours used the closest matching, appropriately reddened P98 library spectra in the r' and i' bands, rather than the calibrated observations, in order to: smooth errors due to irregularities in the spectrophotometric flux calibration; avoid the need to correct for telluric absorption; and provide a good extrapolation of the observed SEDs to cover the full spectral range. Only the H α fluxes were computed by multiplying the H α filter profile directly with the calibrated ISIS spectra.

Both the original IPHAS colours and the colours derived from the fits to the spectrophotometry are listed in Table 5. As there is not yet a uniform and fully verified zero-point calibration for all IPHAS frames, we have to shift the SED-based colours on to the IPHAS colours. The shifts that minimize the mean differences in each of $(r' - H\alpha)$ and $(r' - i')$ are –0.14 and +0.03, with final rms devi-

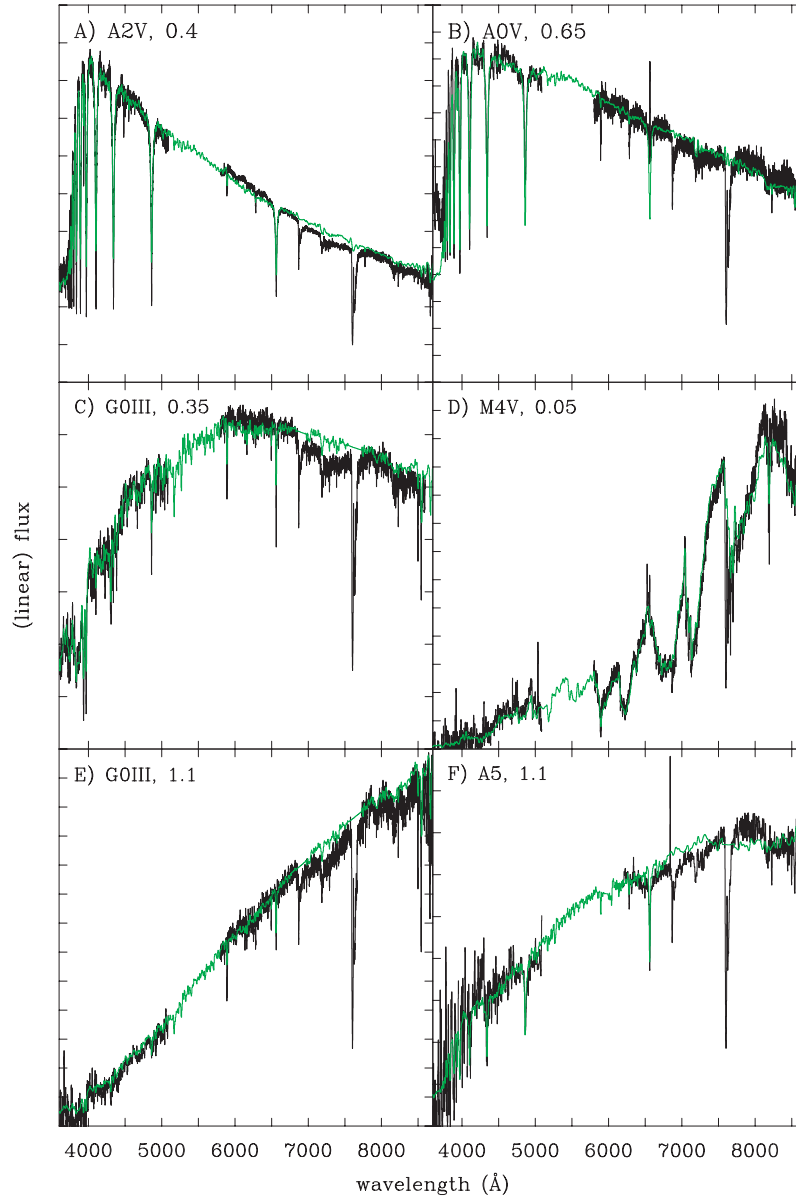


Figure 10. Fits of P98 library spectra (green) to flux-calibrated WHT/ISIS spectra (black) of selected stars in IPHAS field 2540/2540o in Taurus. The label in each box (letters A to F) refer to the positions marked in the colour–colour diagram for this field (Fig. 9). Next to each label is the spectral type and colour excess $[E(B - V)]$ estimate for the star. In each plot, the flux scale is linear, with zero as the minimum plotted value. The ISIS spectra are uncorrected for telluric absorption.

Table 5. Observed and derived properties of the follow-up sample of stars in IPHAS fields 2540/2540o in Taurus.

	IPHAS name/position J[RA(2000)+Dec.(2000)]	IPHAS photometry			Spectral type	$E(B - V)$	Synthetic colours		Comment
		r'	$r' - i'$	$r' - H\alpha$			$r' - i'$	$r' - H\alpha$	
A	J053430.11+251400.9	13.19	0.33	-0.07	A2 V	0.40	0.32	0.09	
B	J053432.14+252231.0	15.82	0.54	0.12	A0 V	0.65	0.47	0.26	H α emission
C	J053425.99+250843.1	13.01	0.61	0.16	G0 III	0.35	0.61	0.30	
D	J053458.93+252316.7	17.22	1.91	0.78	M4 V	0.05	1.86	0.92	
E	J053311.04+251444.5	15.36	1.15	0.30	G0 III	1.10	1.11	0.42	
F	J053305.64+251837.6	17.06	0.86	0.13	A5	~ 1.1	0.84	0.25	Noisy ISIS data

ations between the six pairs of observed and predicted colours of 0.015 and 0.026, respectively. The size and sense of shift in $(r' - H\alpha)$ is as expected (see Section 3). That the shift in $(r' - i')$ is small, but apparently finite, indicates that the night the IPHAS imaging

was obtained was not perfectly photometric. On the basis of the errors estimated for the IPHAS photometry (see Fig. 2), we would expect the rms deviations between the catalogued and observed colours to be ~ 0.01 . The somewhat larger values of 0.015 and 0.026

obtained here turn out to be determined mainly by errors in the relative spectrophotometry and its analysis: for example, the uncertainty in the $E(B - V)$ estimates is typically 0.05 and translates into an $(r' - i')$ error of ~ 0.03 . In $(r' - H\alpha)$, the discrepancies are smaller and mainly arise in the r' -band integration. The circle from photometry to spectroscopy, back to photometry, closes satisfactorily.

At the end of this process, it can be seen in Fig. 9 that star A (A2 V) falls a little below the early A reddening line, rather than just above, while the reddening line itself lies ~ 0.02 mag above the bottom edge of the main stellar locus. A part of the reason for this may be illustrated in Fig. 11 where the P98 A2 V spectrum is superimposed on the ISIS observation of star A: it is possible that the limited resolution of the P98 library spectra ($R \simeq 500$ or $\Delta\lambda \simeq 13 \text{ \AA}$ at $H\alpha$) leads to the $H\alpha$ in-band fluxes of early A-type stars being overestimated, very slightly. Another factor will be linked to the question of the mean $H\alpha$ absorption EW and its variance for early A stars as a function of subtype and metallicity. The $H\alpha$ absorption EW for star A is $14.5 \pm 0.4 \text{ \AA}$, while that for the P98 A2 V star is $10.8 \pm 0.5 \text{ \AA}$. These numbers for A2 V may be compared with the P98 A0 V and Hayes (1985) Vega $H\alpha$ EWs, that are both close to

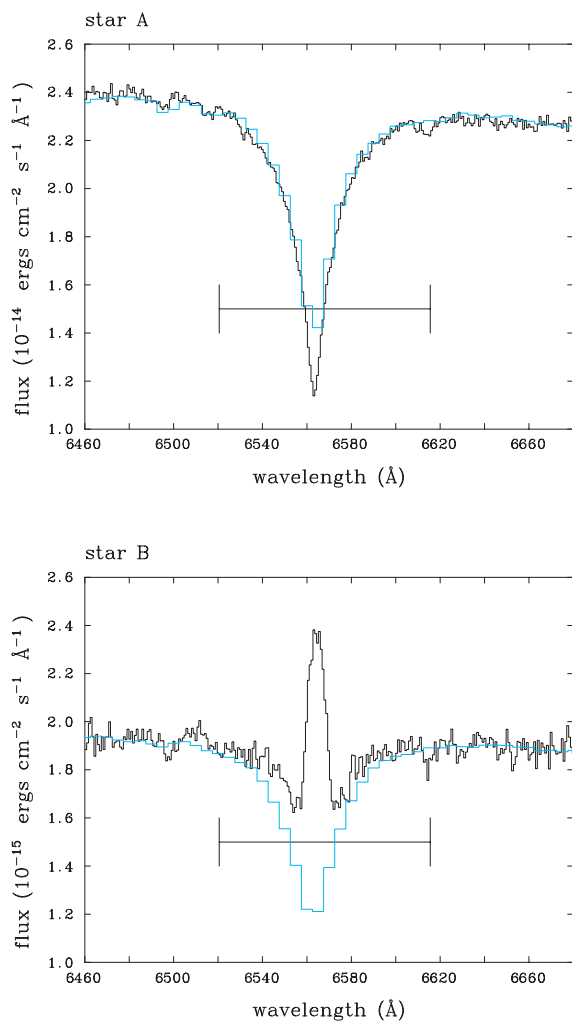


Figure 11. Excerpts of the spectra obtained for stars A and B, focusing on the $H\alpha$ line profiles. The WHT/ISIS observations are plotted in black, while the P98 library spectra of the appropriate spectral types (respectively, A2 V and A0 V) are shown superimposed in blue. The excess emission equivalent width in star B is 12 \AA . In both panels, the positioning and FWHM of the IPHAS $H\alpha$ filter is indicated by the horizontal bar.

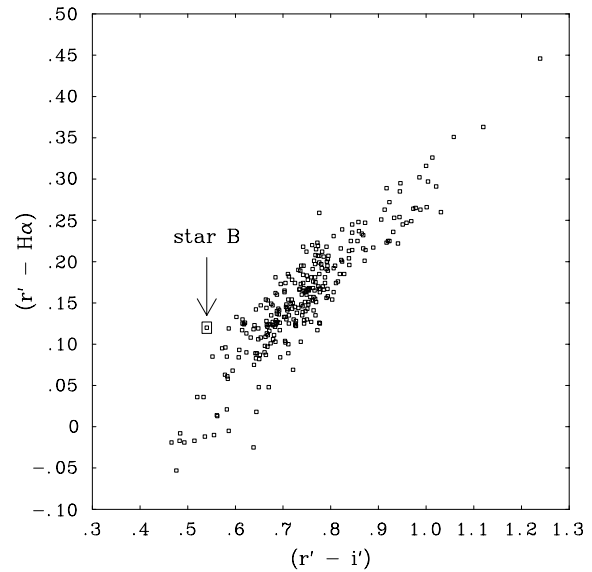


Figure 12. The $(r' - H\alpha, r' - i')$ plane in the locality of star B. The plotted objects are selected with $13 < r' < 19$ and are located in a $10 \times 10 \text{ arcmin}^2$ sky area centred on RA $05^{\text{h}} 33^{\text{m}} 40^{\text{s}}$, Dec. $+25^{\circ} 20' 00''$ (2000). In the absence of its weak $H\alpha$ emission, star B would have fallen 0.13 lower in $(r' - H\alpha)$, at a position typical of non-emission A0 V stars.

13.0 \AA . Finally, we note the contrast between the statement by Jaschek & Jaschek (1987) that the Balmer lines are strongest at A2 (see their table 10.1) and the maximum in P98 for near-solar metallicity dwarfs at A0. The underlying practical difficulty here is the measurement and calibration challenge of the very broad $H\alpha$ absorption wings in A-type spectra. As the IPHAS survey completes and a uniform photometric calibration is constructed, it will then be appropriate to sort the issue out and improve the absolute registration of this lower boundary. For the present, the A0 V spectrum in the P98 library defines the shape of the early A reddening line well enough to allow it to be used in a relative manner.

The $H\alpha$ profile for star B is also presented in Fig. 11. This object shows a distinct central reversal in $H\alpha$, which allows it to be described as a weak emission-line object. The excess (emission) EW with respect to the library A0 V spectrum is 12 \AA . Indeed, it was included in the list of ISIS service targets because of the suspicion that this might be the case: when it is plotted on the colour–colour plane with only neighbouring stars, within a $10 \times 10 \text{ arcmin}^2$ box, it sits clearly separated in $(r' - H\alpha)$ just above the local main stellar locus (see Fig. 12). This is an example of the greater coherence of mean conditions (reddening, nature of population) within a smaller sky area leading to greater success in identifying an ‘unusual’ object.

6 SPECTROSCOPIC TRAWLING FOR EMISSION-LINE AND OTHER RARE OBJECTS: FIELDS IN CEPHEUS

We now present some results from early spectroscopic follow-up of IPHAS in order to give a concrete example of the yields of different object types from IPHAS data. In this case, the choice of sky area has been dictated mainly by observational convenience, rather than by data quality considerations. The results presented here rest on more typical IPHAS photometry.

6.1 The MMT/HectoSpec observations

In 2004 June, we obtained spectra with the Mount Hopkins 6.5-m Multiple Mirror Telescope (MMT) in F/5 configuration using the recently commissioned HectoSpec facility, a multi-object spectrograph fitted with 300 fibres that can be deployed across a field, 1° in diameter (Fabricant et al. 2004). The fibre positioner is mounted at Cassegrain. The 270 groove mm^{-1} grating used delivers broad wavelength coverage (4488–8664 Å) at 6.2-Å resolution. Over two nights, six different fields were observed using two fibre configurations per pointing. The target stars selected for this programme fell mainly in the magnitude range $17 \leq r' \leq 20$. The total on-source exposure times were 1200 s. Spectra were extracted by the instrument pipeline that includes CCD bias and gain corrections, flat-fielding using domeflats as well as a sensitivity correction for the individual fibres using twilight flats. Individual fibre spectra were then extracted and wavelength calibrated using FeNeAr-lamp exposures. Finally, a mean sky spectrum derived from the sky fibres was subtracted. Due to spatial variations in the sky background across the field of view, sky subtraction using sky fibres is not always perfect and care must be taken with spectra displaying weak, unresolved $H\alpha$ emission components. Sky subtraction will be improved in the future using offset sky exposures that sample the sky for each fibre close to the target position, in conjunction with an optimal scaling correction using the strongest sky lines.

6.2 Selecting targets for the Cepheus field

We report the results from one of two pointings in the constellation of Cepheus. Centred on RA $22^{\text{h}}17^{\text{m}}00^{\text{s}}$, Dec. $+61^\circ33'37''$ (2000) ($\ell = 105.6^\circ$, $b = 4.0^\circ$), this position was picked because it contains a strip included in the *Spitzer Space Telescope* Galactic First Look Survey (<http://ssc.spitzer.caltech.edu/fls/galac/>). Despite its relatively high Galactic latitude, this area of sky presents significant and locally variable interstellar extinction (ranging from $A_V \sim 4$ up to ~ 7 mag). This shows up in the IPHAS colour data for the region as somewhat broadened main stellar loci. An example is shown as Fig. 13, where colour data extracted from the IPHAS field pair, 7012/7012o, are plotted. At magnitudes brighter than $r' \sim 19$ (top panel), the colour uncertainties are less than ~ 0.05 and are less significant than environmental factors in the smearing of the main stellar locus: this reverses at fainter magnitudes (lower panel) where the typical errors are ~ 0.1 .

The HectoSpec 1° -diameter field spans then IPHAS field positions, not including offsets. The largest contributions, however, are from IPHAS fields 6985, 6993, 7012 and 7019 (see Table 1). To speed up the compilation of the target lists, we chose to merge the data from all the relevant pointings first, before proceeding to target selection. In merging the data, corrections for photometric shifts between different WFC exposures had to be applied. These were calculated using the mean magnitude offsets for sources located in field overlaps. Inevitably, this merging blurred the main stellar locus in the colour plane some more: compare the lower panel in Fig. 13 with the plot for the full HectoSpec field in Fig. 14. For the future, we are re-ordering the algorithm, in order to give more emphasis to selection at the individual field level (cf. the discussion of ‘star B’ at the end of Section 5). Indeed, a further tactic that can be applied in order to minimize the spread of the main stellar locus is to select from within a number of narrowly set r' magnitude ranges. On this occasion, after merging the catalogues for the relevant individual fields together, the main target selection was performed within the full magnitude range to be observed, $17 \leq r' \leq 20$. Finally, a few

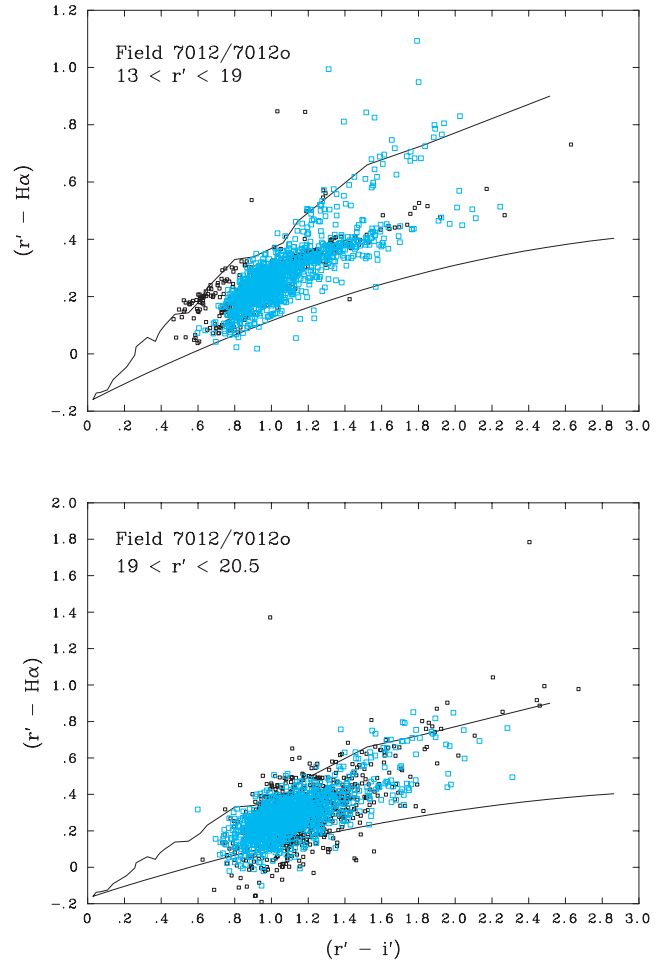


Figure 13. Point-source colour–colour data derived from IPHAS fields 7012/7012o in Cepheus. This plot illustrates the quality of data around ($\ell = 105.6^\circ$, $b = +4.0^\circ$) from which we selected targets for multifibre spectroscopy with MMT/HectoSpec. The magnitude range from which HectoSpec targets were selected was $17 < r' < 20$ (blue data points in both panels: data outside this magnitude range are plotted as smaller black points). The black lines in both panels are the simulated unreddened main-sequence track and early A reddening line, shifted downwards in $(r' - H\alpha)$ by 0.16 mag. Here, they serve as fiducial lines to show how the errors grow at fainter magnitudes.

promising emission-line star candidates down to $r' = 20.5$ were added by hand.

The goal of this first round of HectoSpec observations was to explore the complete IPHAS colour–colour plane while trying to give high priority to objects that are outliers or near the edge of the general distribution of objects. This naturally includes all emission-line star candidates, which lie above the main stellar locus.

To achieve this sampling, the following selection algorithm was applied. The colour–colour plane was split into boxes of 0.1 mag in width and height. Targets were then selected based on the number of objects in each box: from one to three objects in a box, all were selected and given the highest fibre allocation priority; between four and nine objects in a box, a random selection of 75 per cent of the box members was chosen with a slightly lower fibre allocation priority; between 10 and 50 objects, a random fraction falling linearly from 50 to 10 per cent was selected and given a low fibre selection priority based on the number of objects in the box; >50 objects in a box, 10 per cent of the objects were selected randomly and given a low

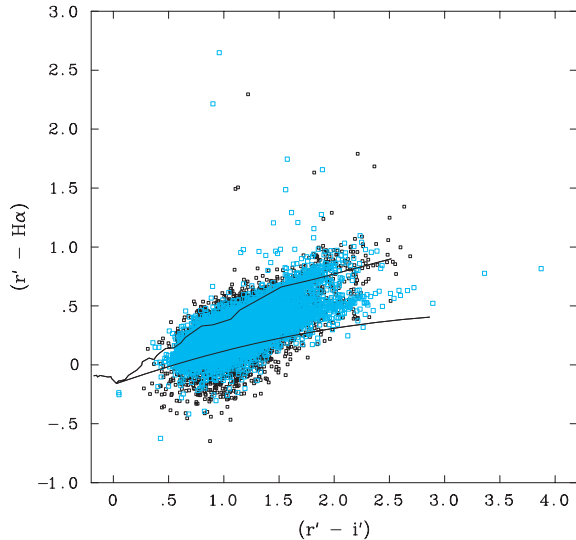


Figure 14. The point-source colour–colour diagram used for target selection in the 1° -diameter field in Cepheus observed with MMT/HectoSpec. Data for objects in the magnitude ranges $17 < r' < 20$ and $20 < r' < 20.5$ are shown in blue and black, respectively. Because of IPHAS field merging and the accompanying ad hoc photometric corrections, the main stellar locus is more diffuse here than in individual field extractions (cf. Fig. 13). The simulated unreddened main-sequence track and the early A reddening line (drawn as solid lines) are accordingly less useful in decoding the data.

fibre selection priority based on the number of objects in the box. The maximum number of objects that could be selected in a box was capped at 10. Finally, if a box had four neighbours in the cardinal directions with 10 or more objects, then only one object was selected for spectroscopy. This rule was introduced to further reduce the number of objects picked for spectroscopic follow-up that lie in the densest (and probably most uninteresting) parts of the stellar distribution.

If the selection algorithm gave less than the requested number of objects (~ 700 for two HectoSpec configurations) then one object per box was added, starting with the least populated boxes until the required number of objects was reached. If more than the requested number of objects was chosen, then one object was removed from each box with more than one object selected: starting with the most populated box until the requested number of objects was reached. By this means, we were able to assign fibres to between 450 and 540 targets, depending on the field observed. Each set was then split into two configurations.

The outcome of this process and the HectoSpec observation of the Cepheus field was a collection of 496 stellar spectra.

6.3 Results of the MMT/HectoSpec spectroscopy in Cepheus

First and foremost, we find that essentially every target star located in the colour–colour plane clearly above the main stellar locus is confirmed as an emission-line star. Altogether, 29 objects are confirmed as having H α in emission, with six or seven lying on or just below the upper bound of the highly populated region (green encircled points in Fig. 15). The one object not encircled in green, at $(r' - i') \simeq 1.1$ and $(r' - H\alpha) \simeq 1.5$, is probably an emission-line object also, but remains ambiguous because it is very faint and its spectrum is correspondingly noisy. There is a still larger group, numbering 47, of probable dMe stars. They are ‘probable’ because

the sky subtraction may have left a false residue of H α emission. The range of H α emission EWs in this group is from a few up to 10–20 Å. Quite plausibly, most of these objects lie mixed in with non-emission dwarf M stars (of which there are 90 or more). The one ‘probable dMe’ star [at $(r' - i') \simeq 2.50$, $(r' - H\alpha) \simeq 1.3$] above the main locus can be viewed as dMe with the greatest confidence because time-variable H α emission is characteristic of dMe stars: presumably at the time of the IPHAS imaging, its H α emission was brighter than 9 months later, at the time of the spectroscopy.

The combination of moderate spectral resolution and short exposure time has meant that many of the more routine objects, without H α in emission or in marked absorption, are more challenging to sort into spectral classes. This large group of 214 objects will be dominated by late-A to mid-K stars, but will also include some non-emission OB stars. The spectra of a further 89 stars are so faint and noisy that no comment can be made about them. The stand-out objects towards the lower boundary of the main stellar locus in Fig. 15 are the stars with H α strongly in absorption. There are 15 of these. Two of them are well separated from the main locus at much lower $(r' - i')$ and also much lower $(r' - H\alpha)$: they are both white dwarfs. Similarly placed objects in other IPHAS fields for which we have MMT/HectoSpec spectra have turned out to be white dwarfs too. The remaining 13 stars with strong H α absorption are early A stars. Tighter classification at this time is not feasible.

We now present a selection of eight objects and their spectra for more detailed discussion. These are identified in the colour–colour plane shown as Fig. 15. The data on them, given in Table 6, include estimates of their r' magnitudes and $(r' - i')$, $(r' - H\alpha)$ colours derived from the highest quality IPHAS exposures currently available. Note that the colours are, typically, different from those plotted in Fig. 15: this is due to the colour shifts applied in combining IPHAS fields before MMT/HectoSpec target selection. Because they assist in assigning broad object class, we also include in the table 2MASS ($J - H$), $(H - K)$ colours and K magnitudes.

Stars 1–3 (Fig. 16) are most likely to be young stellar objects (YSOs) of Herbig or T Tau type. This object class assignment is easiest for star 1 because the veiling is not so extreme as to hide the underlying M-star spectrum. Indeed, a comparison between stars 1 and 4 in Fig. 16 suggests that the M spectral subtypes of these objects are likely to be very similar. The sky around star 1 has been imaged in all four Infrared Array Camera (IRAC) bands by the *Spitzer* Galactic First Look Survey. We downloaded the calibrated images from the *Spitzer* Science Archive and carried out point-source extractions. Star 1 was detected at 3.6, 4.5 and 5.8 μm , with fluxes corresponding to magnitudes of 12.47 ± 0.11 , 12.12 ± 0.12 and 11.93 ± 0.14 , respectively. Using the observed IPHAS, 2MASS and IRAC fluxes, we find that the SED of star 1 from the r' band to 5.8 μm happens to fit quite well to a 2000 K blackbody (although the SED must include components due to a reddened stellar photosphere, an accretion disc and warm dust).

Star 2 has the highest contrast and richest emission-line spectrum of the three stars: in this object, even the Na I D lines are thrown into emission and some forbidden line emission is present. Star 3 is intermediate between 1 and 2, both in terms of the contrast of its emission spectrum and that it is just possible to pick up late-type photospheric absorption against the continuum (e.g. the blend at 6495 Å strong in G/early K stars). The NIR colours of all three objects imply modest NIR continuum excesses that are not out of place for Herbig or T Tau stars, with star 2 showing the most marked excess.

It seems likely that these stars 1–3 are associated with LDN 1188 ($\ell = 105.7$, $b = +4.2$), a dark cloud less than 2° away from the

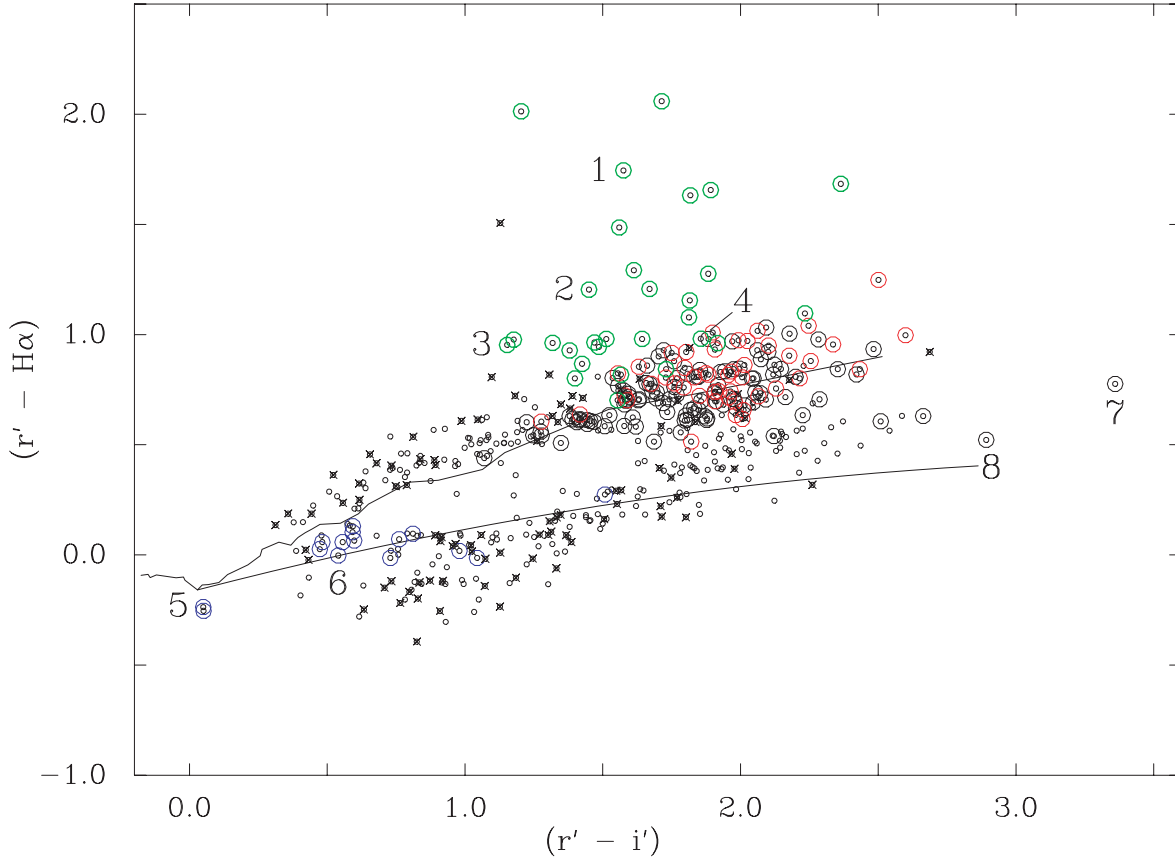


Figure 15. The colour–colour diagram of the Cepheus targets observed with MMT/HectoSpec. Symbols used: each small black circle locates the IPHAS colours of an object for which we have a spectrum; larger green circles pick out confirmed emission-line stars; red circles pick out weaker-emission, possible dMe stars; larger black circles indicate non-emission-line late-type stars with strong molecular bands in their spectra; blue circles pick out stars with prominent H α and H β absorption features; black crosses mark those objects for which the spectrum is too noisy to classify. Small black circles left unadorned will mainly represent late A to early K stars. The synthetic tracks, drawn as solid lines are as in Figs 13 and 14. Spectra of the objects 1–8 are shown in Figs 16 and 18 and parameters on them are given in Table 6.

Table 6. Positions, magnitudes and colours for the eight stars, observed using MMT/HectoSpec, whose spectra are plotted in Figs 16 and 18. The r' magnitudes and $(r' - H\alpha)$, $(r' - i')$ colours have been taken from the catalogues for the best pair of IPHAS exposures. At this time, the magnitudes are likely to be correct to within ± 0.1 mag, while the H α EWs are reliable to within ± 5 Å. The EW sign convention is reversed in that a positive value implies net emission.

	IPHAS name/position J[RA(2000)+Dec(2000)]	IPHAS colours/magnitudes			Object type	2MASS colours/magnitudes			H α EW (Å)
		r'	$r' - i'$	$r' - H\alpha$		$(J - H)$	$(H - K)$	K	
1	J221734.39+611409.2	19.5	1.55 ± 0.06	1.72 ± 0.06	T Tau star	1.22 ± 0.07	0.67 ± 0.05	13.39 ± 0.03	190
2	J221740.30+614702.9	17.7	1.44 ± 0.01	1.42 ± 0.01	B[e]/YSO	1.33 ± 0.04	0.98 ± 0.04	10.52 ± 0.02	200
3	J221411.60+612606.7	17.5	1.15 ± 0.01	0.99 ± 0.01	Be/T Tau	1.38 ± 0.08	0.92 ± 0.05	12.12 ± 0.03	80
4	J221427.30+612943.6	19.5	2.01 ± 0.08	1.08 ± 0.08	\sim M3 Ve	1.09 ± 0.04	0.56 ± 0.04	13.15 ± 0.02	70
5	J221534.47+615725.4	17.2	0.06 ± 0.01	-0.23 ± 0.01	White dwarf	–	–	–	–34
6	J221345.86+614418.6	17.5	0.53 ± 0.01	0.00 ± 0.01	Early A star	0.3 ± 0.2	~ 0.5	~ 15.3	–16
7	J221822.09+614803.8	18.7	3.39 ± 0.03	0.78 ± 0.04	Mid-M giant	1.66 ± 0.04	0.62 ± 0.04	8.68 ± 0.02	
8	J221619.89+612621.1	19.5	2.97 ± 0.06	0.71 ± 0.07	Carbon star	2.61 ± 0.03	1.76 ± 0.03	6.41 ± 0.02	

well-known Sh 2-140 region of star formation. This proximity suggests a similar distance to both regions, which has been given as 910 pc for Sh 2-140 by Crampton & Fisher (1974). However, both these nebulae lie on the periphery of Cep OB2, to which the distance appears to be rather less (~ 600 pc, de Zeeuw et al. 1999). In a study of LDN 1188, Abraham et al. (1995) reported the discovery of a number of emission-line stars in objective prism data obtained at Konkoly Observatory at brighter magnitudes than our

HectoSpec selection. RNO 140 and 141 (Cohen 1980) are also in this neighbourhood.

Star 4 can be presumed to be in the foreground with respect to LDN 1188 and stars 1–3. Hence, its JHK colours, combined with its spectral type can be used to estimate a minimum interstellar extinction towards LDN 1188. This works out at $E(B - V) \simeq 1.3$ or $A_V \simeq 4$ (for $R = 3.1$ and using data from Bessell & Brett 1988). We can now see if this marries up with the implications of

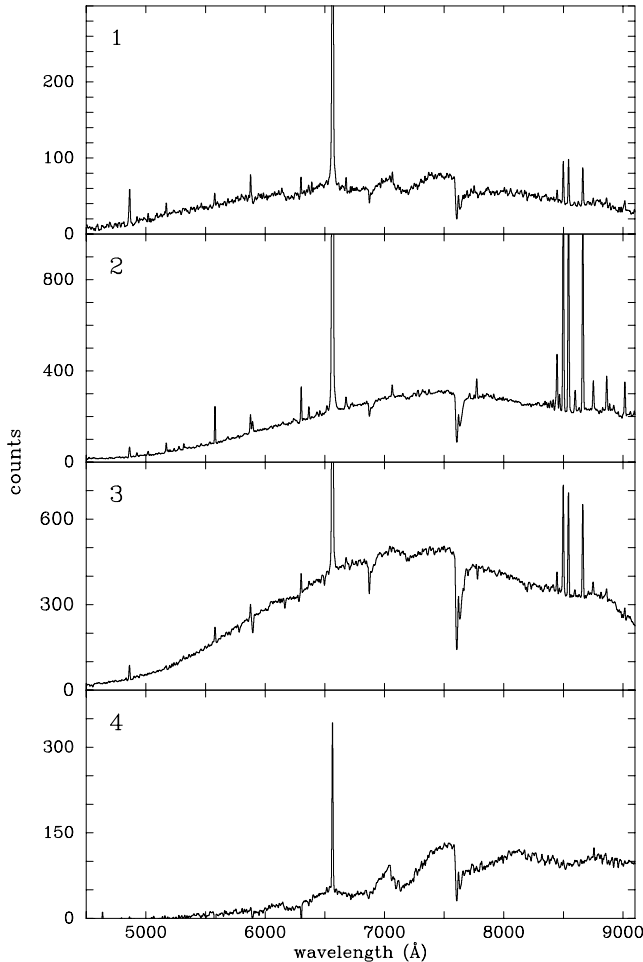


Figure 16. The MMT/HectoSpec counts spectra of Cepheus targets 1 to 4, as marked in Fig. 15 and listed in Table 6. These data and those shown in Fig. 18 are uncorrected for telluric absorption.

the IPHAS colours of stars 1–3 by comparing their catalogue values with reddened synthetic estimates. This is accomplished via Fig. 17 in which the IPHAS colours for stars 1 to 3 (Table 6) are compared with synthetic tracks (Table 4).

If star 2, with its generally high contrast emission-line spectrum is a Herbig or T Tau star with an accretion dominated SED, its reddening would correspond to $E(B - V) \simeq 2$: for, in Fig. 17, it lies just to the right of the track for $F_\lambda \propto \lambda^{-2.3}$ and $E(B - V) = 2$. A similar, or somewhat lower, reddening would appear plausible for star 1 in that its optical SED should be somewhat redder, intrinsically, than that of star 2. The intrinsic optical SED of star 3 should be intermediate between stars 1 and 2 (given the marginal detection of late-type photospheric absorption), and yet it is observed to be ‘bluer’ than either. The highest likely reddening of star 3 is $E(B - V) \sim 1.5$: this reddening would apply in the limiting case of an accretion-dominated SED, where the contribution of the G/K star is small.

On the basis of its $(r' - i')$ colour and spectral type, and after correction for its H α emission, star 4 would be assigned $E(B - V) \simeq 1$. This is a somewhat lower estimate than the estimate based on 2MASS NIR colours [$E(B - V) \simeq 1.3$] but not so large a discrepancy that either the NIR or optical photometrically calibration must be called into question. In conclusion, we find that the order of increasing reddening appears to be: star 4 in the foreground,

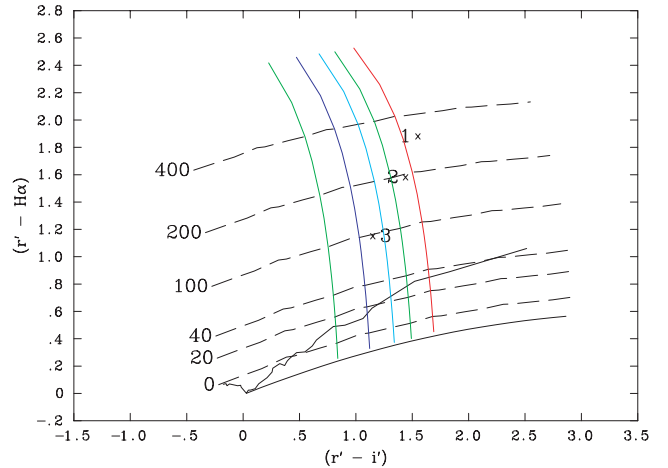


Figure 17. A diagnostic colour–colour diagram for the Cepheus region stars 1 to 3 in Table 6. The blue, light blue, (right-hand) green and red tracks, from Table 4 and Fig. 6, are reddened to $E(B - V) = 2$. They respectively represent the colour–colour response to increasingly strong (narrow) H α line emission of extreme O stars, $\sim A0$ stars, optically thick accretion discs and $\sim G2$ stars. For contrast, the track for optically thick disc accretion at $E(B - V) = 1$ (left-hand green line) is also shown. The horizontal dashed lines are lines of constant H α equivalent width. The numbers 1–3 mark the positions of stars 1–3: note that their $(r' - H\alpha)$ colours have been incremented by 0.16 (cf. Fig. 13) to place them in the simulation colour domain. The required correction in $(r' - i')$ will be significantly smaller.

star 3, and then star 1 and star 2, spanning the range $1 \lesssim E(B - V) \lesssim 2$. The Schlegel et al. (1998) Galactic reddening maps indicate maximal reddenings of $E(B - V) \sim 2.5$ for this part of the plane. We have rough consistency and a first indication of patchy reddening towards the young objects in the vicinity of LDN 1188. If half the r' flux of star 1 is attributed to an $\sim M3$ stellar photosphere and $A_V \sim 6$, one may deduce a stellar radius of around 4 times the M3 V main-sequence radius, for a distance of ~ 600 pc.

The IPHAS colours for stars 2 and 3, picked out in Fig. 17, are broadly consistent with their observed H α EWs (200 and 80 \AA), in that their colours ‘predict’ EWs of ~ 200 and ~ 100 \AA , respectively. Only star 1 is discrepant in that its observed EW (~ 190 \AA) is distinctly low compared with the implications of its IPHAS colours (suggesting an enormous EW of about 250 \AA). Given that the H α EW is well known to be a time-variable quantity in most classes of emission-line object, consistency for two out of three objects is acceptable.

The spectra of four non-emission-line objects, stars 5–8, are shown in Fig. 18. These draw attention to what can be called H α deficit positions in the IPHAS colour–colour plane (cf. Fig. 15). At the blue end, objects 5 and 6 are examples of extreme and strong H α absorption objects: respectively, a white dwarf and an early A star. At the red end, objects 7 and 8 are respectively a normal, somewhat reddened mid-M giant, while object 8 has the distinctive CN band structure of a carbon star in its spectrum. Object 7 is typical of the stars populating the red end of the giant strip in the IPHAS plane. The NIR colours and rough spectral type ($\sim M4$ III) suggest a reddening corresponding to $E(B - V)$ of about 2. Carbon stars like object 8 will usually fall below the red giant strip (lacking the TiO bands that, in M-type spectra, lead to the seeming flux maximum in the H α region). In terms of its NIR colours, star 8 is a more extreme object than the suspected carbon star mentioned at the end of Section 5 [although reddening gives both objects more

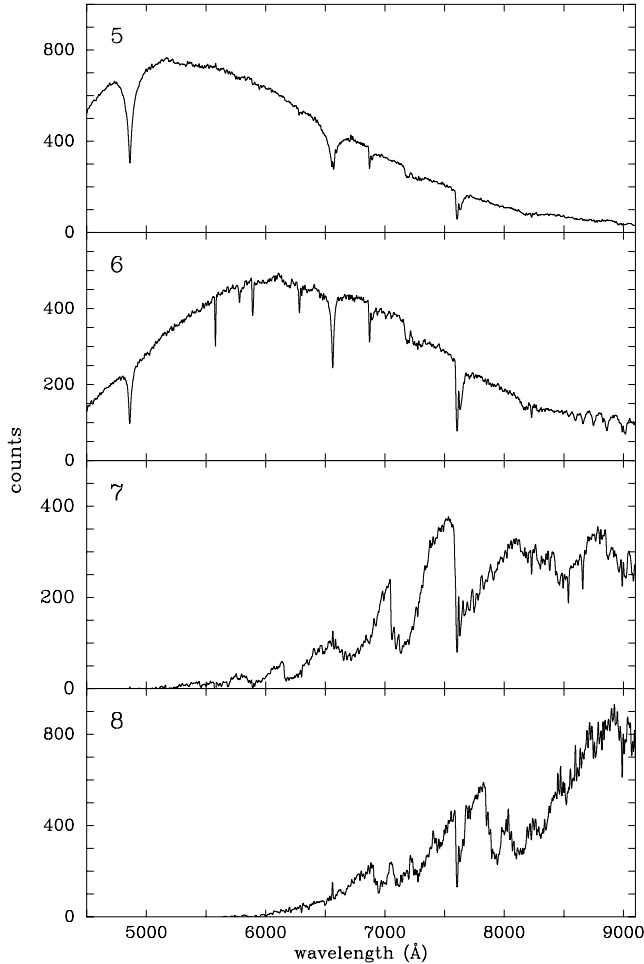


Figure 18. The MMT/HectoSpec counts spectra of Cepheus targets 5 to 8, as marked in Fig. 15 and listed in Table 6.

extreme ($J - H$, $H - K$) colours than seen in the local Galactic carbon star sample of Claussen et al. 1987]. Indeed, object 8 appears to be a reddened ($A_V \sim 5$) version of 2MASS J0326599+143957, described by Liebert et al. (2000) as a luminous, very cool, late N type carbon star.

In summary, our early MMT/HectoSpec observations of this field in Cepheus sample a diverse range of objects. Sources lying clearly above the stellar locus in the ($r' - H\alpha$, $r' - i'$) colour–colour plane have indeed been confirmed as true emission-line objects with $H\alpha$ EWs ranging from a few to 200 Å. Many of them are likely to be Herbig or T Tau stars. In addition, several $H\alpha$ deficit sources have been identified. Multi-object spectroscopic follow-up will remain a key part of our efforts to mine the IPHAS data base.

7 IPHAS OPPORTUNITIES FOR $H\alpha$ IMAGING

The power of the survey for detecting stellar $H\alpha$ emission has already been described. A second target for the survey are the spatially resolved emission-line nebulae. These nebulae are (like emission-line stars) associated with early and late phases of stellar evolution, and indicate ionization of circumstellar gas, in the form of H II regions, planetary nebulae and supernova remnants. Already, in the Southern hemisphere, the UKST SHS has shown the remarkable

incompleteness of existing catalogues by doubling the number of known planetary nebulae (Parker et al. 2003).

The Galactic plane shows ubiquitous diffuse $H\alpha$ emission as well as reflection nebulae, which need to be distinguished from circumstellar ionized nebulae. Because reflection nebulae are the product of continuum scattering, they can be removed by comparison of $H\alpha$ and r' images. Diffuse $H\alpha$ emission occurs on large size scales (10 arcmin to degrees) and lacks the usual symmetry of circumstellar nebulae.

Imaging of extended nebulae requires well-behaved background on the CCDs making up the WFC. Because of this, the preferred image properties for nebular studies are very different from those for point-source extraction: high background is acceptable for the latter, while poor seeing is acceptable for the former. Small nebulae covered well within a single CCD do not require special reduction. Each object will usually have been covered in at least two pointings by the time the survey is complete, giving improved signal-to-noise ratio (S/N). For larger objects, mosaics need to be made. Subtracting an r' frame removes stars: for small areas this can be done using PSF matching techniques, but this is very computationally intensive: such that, for larger fields, a direct subtraction is used, although this typically leaves larger residuals.

The limitations of the technique are largely due to background variations. The observations are generally taken in grey and bright time. Different fields will therefore present very different background sky levels. The sky subtracts fairly well in an $H\alpha - r'$ image (unless the background is variable under non-photometric conditions), but if there is smooth extended $H\alpha$ emission over large angular scales, its contribution is currently not separately determined from the sky contribution. Internal reflections are seen in some images, from bright stars. In some locations, a bright star just outside the field of view gives a flare-like feature on the edge of a nearby frame.

A photometric calibration is determined for point sources, but not for extended emission. To correctly calibrate emission nebulae, assuming the continuum background is fully subtracted, the filter response curve needs to be precisely known and needs to be stable over the likely Doppler wavelength shifts (Ruffe et al. 2004). [N II] will also intrude into the flux. Currently, calibration is best performed using known planetary nebulae located in the imaged area. Note that stellar $H\alpha$ sources cannot be used for calibration as their line flux tends to be time variable.

7.1 A supernova remnant

As an example of the possibilities regarding extended nebulae, we present an image of the supernova remnant S 147 (Shajn 147, or Simeis 147, in full: not Sh 2-147, with which it is confused in the SIMBAD data base). This is a near-perfect remnant of an approximately spherical shape, showing a typical filamentary structure. It is positioned just overlapping the antigalactic centre, its own centre being at $\ell \simeq 180.1^\circ$, $b \simeq -1.6^\circ$. However, due to its large extent, spanning several degrees, only photographic images have been published so far (Van den Bergh, Marscher & Terzian 1973). See also the 2005 March 24 ‘Astronomy Picture of the Day’ by R. Gendler (<http://antwrp.gsfc.nasa.gov/apod/ap050324.html>).

An IPHAS image of S 147 was produced by combining approximately 250 pointings. The pipeline mosaicking procedure was found to be inadequate for combining many fields taken under widely varying conditions. We therefore used the pipeline only to produce reduced images of the individual CCDs for each pointing. Then, for each image, we subtracted the r' image from the $H\alpha$ data and

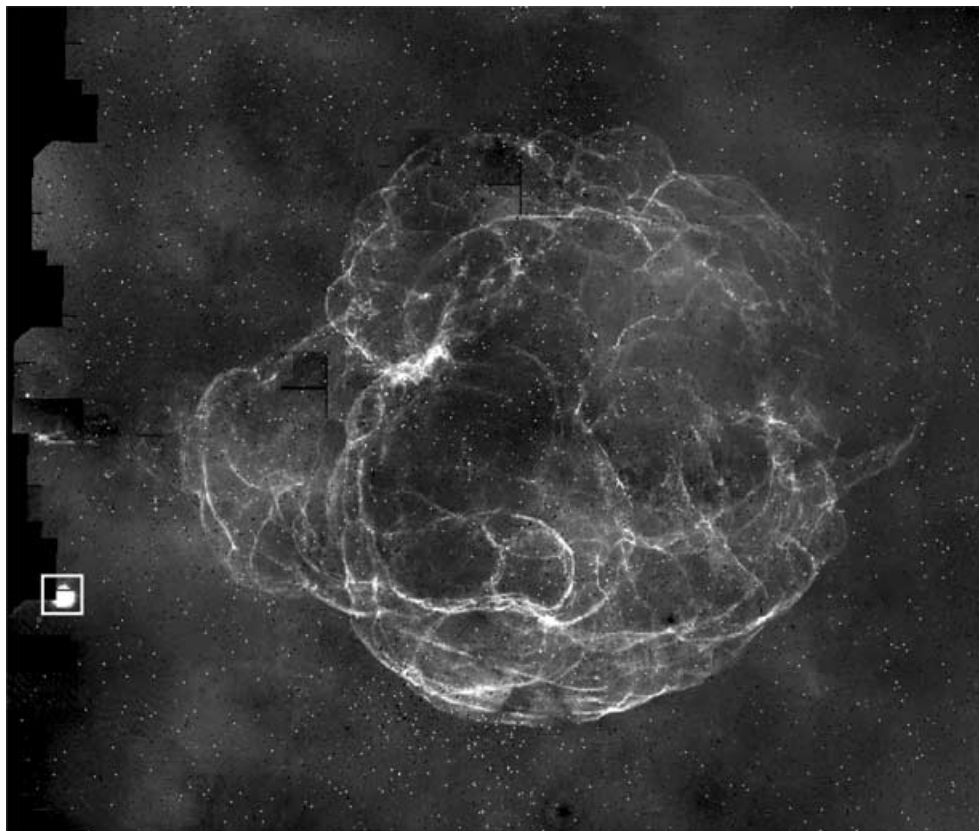


Figure 19. The continuum-subtracted H α image mosaic of the extremely large angular size supernova remnant, S 147. The frame size is roughly 5° across and 4° down. The extent of the supernova remnant is given by Van den Bergh et al. (1973) as 200×180 arcmin 2 . N is up and E to the left. The H II region, Sh 2-242, is picked out near the eastern edge of the image by the white box (see Fig. 20).

smoothed to a pixel size of 5 arcsec (a binning factor of 15). The background per image was approximately nulled by subtraction of the median: in fields with bright and extended emission this required manual selection of areas for background definition: otherwise the median over all four CCDs of one pointing was used. One corner of CCD no. 3 is affected by scattered light in conditions of bright Moon light (amplified if cirrus was present): this corner was always blanked out. All CCDs tend to show a gradient along the long axis of about 1 ADU in the subtracted image: this could be due to a charge-transfer efficiency limitation, but its exact cause is not known. It does not subtract automatically because the r' image is scaled first: accordingly, as a final step, this remaining gradient was subtracted from all images.

The resulting images were combined in a single mosaic using the Virtual Observatory software package MONTAGE. This involved regridding each frame and determining background corrections by comparing areas in common between different images. We finally produced an image covering 25 deg^2 . We note that extended emission on scales of a degree or more may not be well represented, as it can be affected by the background subtraction procedure. However, the filamentary structures are very well recovered. The background fitting was found to be insufficiently constrained at the outer edges of the imaged area, leaving some negative areas. To deal with this, a linear gradient was fitted to the background in empty regions of the full field and subtracted.

The image of S 147 is shown as Fig. 19. A bigger version is to be found in the ING Newsletter article describing IPHAS (Drew et al. 2005). The improvement is very marked in comparison with

the photographic image shown by Van den Bergh et al. (1973): the huge increase in dynamic range brings with it a subtlety of detail missing from the old imagery. Furthermore, these data allow smaller areas to be imaged to much higher resolution. However, even at this 5 arcsec rebinning, the structure is clear. We note that a blow-out is obvious on two sides of the remnant: left and right (to the E and W). The full extent of S 147 is essentially as reported by Van den Bergh et al., at a mean diameter of just over 3° : several times that of the Moon.

At the eastern edge of the image mosaic and south of centre lies another prominent but much more compact nebulosity, Sh 2-242. This very bright smudge in Fig. 19 has a mean H α diameter of 8.0 arcmin. As a contrast to the very large scale structure of S 147, we show as Fig. 20, a full resolution image of this H II region.

8 SUMMARIZING DISCUSSION

The main aim of this paper has been to introduce IPHAS. By the beginning of 2005, 55 per cent of the imaging observations had been obtained. It is expected that the survey will reach completion in 2006.

Given that previous surveying of the northern Galactic plane for emission-line objects rarely reached deeper than $V \sim 13$ (see KW99), while the sensitivity limit of IPHAS is $r' \sim 20$, there is no doubt that a huge domain is being opened up for exploration for the first time. It is difficult to predict the numbers of emission-line objects that will be discovered, even now with the survey in progress, because the distribution of such objects along the Galactic plane is

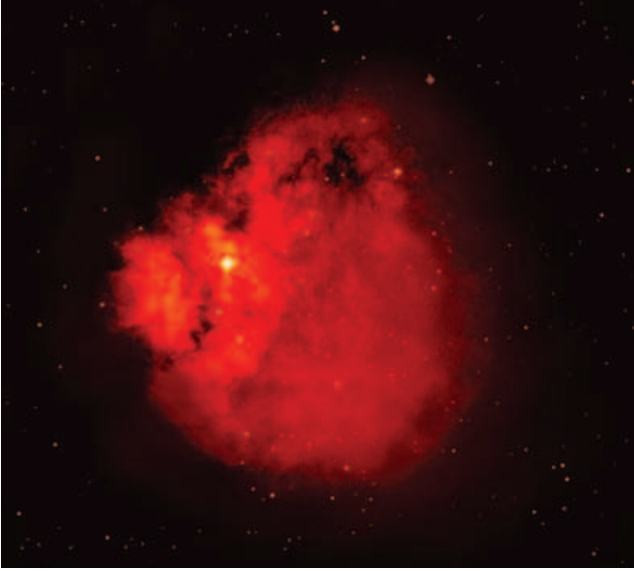


Figure 20. The H II region, Sh 2-242, picked out on the eastern edge of Fig. 19, shown at full resolution. This is a false colour composite of the images in the three filters. The imaged area is roughly 10×10 arcmin². N is up and E to the left.

extremely uneven (see KW99). The small number of IPHAS fields discussed in this paper fit in with this impression: no emission-line objects were evident in the colour–colour plane for the Taurus field (2540/2540o in Section 5: however, a very modest example was found on closer examination); a handful were evident in the Aquila fields (Section 4) and upwards of 20, all fainter than $r' = 17$, were picked up in the MMT/HectoSpec pointing towards LDN 1188 in Cepheus (Section 6). Crudely averaging the experience to date, it is likely IPHAS will uncover around 10 emission-line objects per deg² in the range $13 < r' < 20$ (roughly two to three per IPHAS field) and hence no less than $\sim 20\,000$ altogether.

Through its use of both narrow-band H α and broad-band r' and i' CCD photometry, IPHAS has the capability to pick out H α deficit objects: a possibility typically beyond objective prism spectroscopy, the traditional tool of emission-line star hunting. For example, unreddened white dwarfs are easily spotted as blue objects with small or negative $(r' - H\alpha)$, separated from the main stellar locus in the IPHAS $(r' - H\alpha, r' - i')$ plane. It is a reasonable guess that over 1000 will be discovered in IPHAS data, just as have been discovered in a comparable sky area around the north Galactic cap via the Sloan survey (Kleinman et al. 2004). Very red H α deficit objects can be either brown dwarfs or carbon stars [classes of star that both lack the TiO band absorption responsible for raising $(r' - H\alpha)$ in normal M stars], or they can be very reddened, rare examples of late-type supergiants. Two carbon stars (one probable, the other confirmed) have been reported here.

A further role for IPHAS is that it can help trace the way in which the stellar populations making up the Galactic plane vary across the northern sky. It has been shown here that not all sight-lines look the same in IPHAS colours: of particular note is the sharp contrast between the red giant deficient Taurus field ($\ell = 181.7^\circ$, Section 5), in the Galactic anticentre region, versus the Aquila fields ($\ell \simeq 33^\circ$) with their prominent giant-star populations, sampling the inner Galaxy. Before now, rather little has been known about the far reaches of the Milky Way outside the Solar Circle. For example, the recent study of Galactic spiral structure by Russeil (2003)

reaches only to ~ 6 kpc, outwards from the Sun. The sensitivity of IPHAS is more than adequate for extending our knowledge much further: even relatively humble A0–A3 V stars (easily picked out around what has been dubbed the early A reddening line in the IPHAS colour–colour plane) are potentially accessible out to distances of ~ 20 kpc in the direction of the lightly reddened Galactic anticentre.

We have laid out the character of the $(r' - H\alpha, r' - i')$ colour–colour plane that is unique to this survey and have established a grid of simulated colours that will be of use in the analysis of IPHAS observations. In doing this, we have inevitably identified items of work for the future. For example, a job remains to be done to achieve as good a quantitative match between simulations and observations of M stars as is achieved for earlier spectral types. A related problem has been noted by those developing Sloan Digital Sky Survey photometric calibrations (Smith et al. 2002). The reward for solving this problem will be the chance to fully realize the potential of IPHAS as an unparalleled resource for the statistical analysis of M-dwarf activity. Another task is to gather a range of early A star spectra that can be used to achieve better definition of the early A reddening line and its dependences. As specified here, it is unlikely to be more than ~ 0.02 mag from its correct registration in $(r' - H\alpha)$.

Bigger issues to be dealt with are that the photometric calibration of IPHAS data will need to be made uniform across the survey and that a proper definition of H α magnitude zero-point (referred to Vega) is needed that can be applied within the pipeline processing. Until these calibration requirements have been met, it will remain necessary to derive colour offsets between observed and simulated data independently for every IPHAS field. Typically, offsets in $(r' - i')$ will be small: however, for $(r' - H\alpha)$, the differences between catalogue and simulated colours may vary from ~ 0.1 up to ~ 0.2 mag. In most cases, it is easy to gauge the required offset by matching the synthesized unreddened main-sequence track and early A reddening line to the upper and lower boundaries of the main stellar locus in the colour–colour plane.

Simulations have also been performed that show how the EW threshold for the detection of H α emission will change with observed $(r' - i')$ colour (Section 3.2 and Fig. 6). The photometric accuracy of IPHAS is such that $(r' - H\alpha)$ differences of 0.05–0.1 are significant down to $r' \sim 20$. Re-expressed in terms of an H α EW and for magnitudes brighter than ~ 19 , this corresponds to a threshold emission EW of roughly 5 Å.

It has been shown that the typical morphology of the main stellar locus in the colour–colour plane permits the selection of candidate emission-line stars with threshold H α emission at low $(r' - i')$ only. In practise, the IPHAS bright magnitude limit ($r' \sim 13$) has the effect of all but eliminating normal stars with colours bluer than $(r' - i') \sim 0.5$ from the point-source catalogue (note Figs 3, 9 and 14): with the consequence that lightly reddened subluminescent accreting objects, with or without H α emission, will usually lie comfortably outside the main stellar locus. IPHAS can therefore be used straightforwardly to identify all such objects (in addition to many non-interacting white dwarfs, found as ‘deficit’ objects).

The threshold for H α emission high-confidence detection rises from ~ 10 Å EW at $(r' - i') \sim 1$ up to ~ 50 Å at $(r' - i') \sim 2.5$: beyond this, the colour–colour plane typically becomes sparsely populated again. This has important implications for the detectability of T Tau and other young emission-line objects: based on EW data collected by Reipurth, Pedrosa & Lago (1996, their table 1 and fig. 10), one-third to a half of such objects would be immediately identifiable as emission-line objects in the IPHAS data base at $E(B - V) \simeq 3$. At lower reddenings, the fraction would be higher.

This suggests that the roles for IPHAS with respect to young stellar populations are (i) finding extreme examples anywhere (here, we have presented two with H α emission EWs of ~ 200 Å) and (ii) picking out new associations through the detection of its most active members. Once a new association is identified, a more detailed exploration of catalogued IPHAS sources, exploiting the tricks of, for example, apparent magnitude binning or small area searches, would be likely to uncover further candidate emission-line sources.

Evolved high-mass stars, with H α emission, that find their way into the IPHAS data base will do so because they are very distant and significantly reddened (they are otherwise too bright). The more extreme, least well-understood, and therefore more interesting groups (Wolf–Rayet stars, luminous blue variables, B[e] stars, yellow hypergiants) usually present very high EW H α emission (~ 100 Å and more) and so will not be missed. The most extreme point-source emission-line objects of all, compact nebulae, are most likely to appear to be relatively blue in ($r' - i'$) or even evade detection in the i' band, and will have the most extreme values of ($r' - \text{H}\alpha$) possible, i.e. not more than 3 to 3.1, in practice.

This connects naturally to a topic only touched on in this paper: the exploitation of IPHAS in the study of spatially resolved nebulae (deferred to a later paper). A search for planetary nebulae is in progress, in which several tens of candidates have been identified and a few have been studied spectroscopically. A paper on the study of an intriguing quadrupolar nebula located well outside the Solar circle is in preparation (Mampaso et al.). Here, we have simply drawn attention to the flexibility IPHAS presents for the investigation of a wide range of spatial scales, ranging from arcseconds to several degrees.

Further power to diagnose either particular object types or complete stellar populations will come from pooling IPHAS r' , H α and i' data with data from surveys in different wavebands. In the future of astronomy conducted via virtual observatories, a survey as comprehensive as IPHAS (with its particular exploitation of narrow-band H α data) will be a major resource. Currently, there is an obvious synergy with the all-sky NIR survey 2MASS, although this is limited to the reddened parts of the northern Galactic plane because 2MASS reaches only to $K \sim 15$. The gap this leaves should soon be plugged by the UKIRT Infrared Telescope Deep Sky Survey (UKIDSS) Galactic Plane Survey, reaching to $K = 19$ (see <http://www.ukidss.org/>). Beyond IPHAS, comprehensive optical surveying of the northern Galaxy using linear detectors is still lacking. However, it is interesting to note the recent release by SDSS of $u'g'r'i'z'$ data on a number of low Galactic latitude fields (Finkbeiner et al. 2004).

We finish with a comment on the plans for making IPHAS data available to the community. At the present time, there is open access to the reduced images held at CASU, from a year after the images have been processed. Accordingly the images obtained in 2003 can already be accessed by anyone able to reach the CASU web interface (<http://apm2.ast.cam.ac.uk/cgi-bin/wfs/dqc.cgi>). Access immediately after processing is available to those working in the ING partner countries: the UK; Spain and the Netherlands. The point-source catalogues are to be released in two stages: in the first half of 2006, we aim to release as many as are available, calibrated only at the individual exposure level (as they have been described here); we intend to follow this up with a second release, after the survey is complete and when a uniform calibration has been established across all fields. We anticipate that the final catalogue will contain photometry on around 80 million point sources, capturing data on roughly one for every 1000 stars estimated as existing in the northern Milky Way.

ACKNOWLEDGMENTS

This paper makes use of data from both the Isaac Newton and William Herschel Telescopes, operated on the island of La Palma by the ING in the Spanish Observatorio del Roque de los Muchachos of the Instituto de Astrofísica de Canarias. The multi-object spectroscopic observations reported here were obtained at the MMT Observatory, a joint facility of the Smithsonian Institution and the University of Arizona. We would like to thank the HectoSpec team for their assistance: in particular, Nelson Caldwell and Perry Berlind for their help with the data acquisition, and Susan Tokarz for the pipeline reduction products. We also acknowledge use of data products from the 2MASS, which is a joint project of the University of Massachusetts and the Infrared Processing and Analysis Center/California Institute of Technology (funded by the National Aeronautics and Space Administration and National Science Foundation of the USA). This research has made use of the SIMBAD data base, operated at CDS, Strasbourg, France. DS acknowledges a Smithsonian Astrophysical Observatory Clay Fellowship.

REFERENCES

- Abraham P., Dobashi K., Mizuno A., Fukui Y., 1995, *A&A*, 300, 525
 Bertelli G., Bressan A., Chiosi C., Fagotto F., Nasi E., 1994, *A&AS*, 106, 275
 Bessell M. S., Brett J. M., 1988, *PASP*, 100, 1134
 Claussen M. J., Kleinmann S. G., Joyce R. R., Jura M., 1987, *ApJS*, 65, 385
 Cohen M., 1980, *AJ*, 85, 29
 Crampton D., Fisher W. A., 1974, *Publ. Dom. Astrophys. Obs.*, 14, 283
 Dame T. M., Thaddeus P., 1985, *ApJ*, 297, 751
 Drew J. E., Barlow M. J., Unruh Y. C., Parker Q. A., Wesson R., Pierce M. J., Mashed M. R. W., Philipps S., 2004, *MNRAS*, 351, 206
 Drew J. E. et al., 2005, *ING Newsletter*, 9, 3
 Fabricant D. et al., 2004, *SPIE*, 5492, 767
 Finkbeiner D. P. et al., 2004, *AJ*, 128, 2577
 Hayes D. S., 1985, in Hayes D. S., Pasinetti L. E., Davis Philip A. G., eds, *Proc. IAU Symp. 111, Calibration of fundamental stellar quantities*. D. Reidel Publishing Co., Dordrecht, p. 225
 Hillebrandt W., Niemeyer J., 2000, *ARA&A*, 38, 191
 Howarth I. D., 1983, *MNRAS*, 203, 301
 Irwin M. J., 1985, *MNRAS*, 214, 575
 Irwin M. J., 1997, in Espinosa J. M., ed., *Instrumentation for Large Telescopes* (Cambridge Contemporary Astrophysics). Cambridge Univ. Press, Cambridge, p. 35
 Irwin M. J., Lewis J., 2001, *New Astron. Rev.*, 45, 105
 Irwin M. J., McMahon R., Walton N. A., González-Solares E., Hodgkin S., Irwin J., Lewis J., 2005, *ING Newsletter*, 9, 8
 Jaschek C., Jaschek M., 1987, *The classification of the stars*. Cambridge Univ. Press, Cambridge, p. 205
 Kleinman S. A. et al., 2004, *ApJ*, 607, 426
 Kohoutek L., Wehmeyer R., 1999, *A&AS*, 134, 255 (KW99)
 Landolt A. U., 1992, *AJ*, 104, 340
 Liebert J., Cutri R. M., Nelson B., Fitzpatrick J. D., Gizis J. E., Reid I. N., 2000, *PASP*, 112, 1315
 Merrill P. W., Burwell C. G., 1933, *ApJ*, 78, 87
 Morgan D. H., Parker Q. A., Russeil D., 2001, *MNRAS*, 322, 877
 Naylor T. J., 1998, *MNRAS*, 296, 339
 Parker Q. A., Morgan D. H., 2003, *MNRAS*, 341, 961
 Parker Q. A. et al., 2003, in Kwok S., Dopita M. A., Sutherland R., eds, *Proc. IAU Symp. 209, Planetary Nebulae: their evolution and role in the universe*. Astron. Soc. Pac., San Francisco, p. 25
 Parker Q. A. et al., 2005, *MNRAS*, in press
 Pickles A. J., 1998, *PASP*, 110, 863 (P98)
 Reipurth B., Pedrosa A., Lago M. T. V. T., 1996, *A&AS*, 120, 229
 Robertson T. H., Jordan T. M., 1989, *AJ*, 98, 1354

Ruffle P. M. E., Zijlstra A. A., Walsh J. R., Gray M. D., Gesicki K., Minniti D., Comeron F., 2004, MNRAS, 353, 796
Russeil D., 2003, A&A, 397, 133
Russeil D., Parker Q. A., 2001, Publ. Astron. Soc. Aust., 18, 76
Schlegel D. J., Finkbeiner D. P., Davis M., 1998, ApJ, 500, 525
Smith J. A. et al., 2002, AJ, 123, 2121
Stephenson C. B., Sanduleak N., 1971, Publ. Warner & Swasey Obs., 1, 1 (SS71)
Uenishi T., Nomoto K., Hachisu I., 2003, ApJ, 595, 1094

Van den Bergh S., Marscher A. P., Terzian Y., 1973, ApJS, 26, 19
Wackerling L. R., 1970, MNRAS, 73, 153
de Zeeuw P. T., Hoogerwerf R., de Bruijne J. H. J., Brown A. G. A., Blaauw A., 1999, AJ, 117, 354

This paper has been typeset from a $\text{\TeX}/\text{\LaTeX}$ file prepared by the author.